Department of Precision and Microsystems Engineering

Early-Stage Design and Analysis of 2D Photonic Crystal-based Lightsails

Wiktor Julian Duda

Report no : 2024.047
Coach : Dr. R.A. Norte, Dr. M.A. Bessa
Specialisation : Dynamics of Micro- and Nanosystems
Type of report : Master Thesis
Date : 2 July 2024

EARLY-STAGE DESIGN AND ANALYSIS OF 2D PHOTONIC CRYSTAL-BASED LIGHTSAILS

MSc Thesis

by

Wiktor Julian DUDA

Student Number: 4749286
Thesis advisors: Dr. R.A. Norte, TU Delft, 3mE faculty
Dr. M.A. Bessa, Brown University

ABSTRACT

The current frontier of human exploration is space. We have achieved sending rovers to planets and probes throughout the Solar System and beyond into interstellar space, yet the stars seemed to be out of reach. The current fastest man-made object would take thousands of years to travel to the nearest star, Proxima Centauri. However, Breakthrough Starshot presents an engineering challenge to reach it in a generation's time. Recent technological advancements make this possible through ultralight spacecraft equipped with mirror-like sails, known as Lightsails. Due to their structure, these sails could be propelled by lasers up to 20% light speed, or over 200 million km/h.

To achieve the required efficiency, the sails need to exhibit high reflectivity and low mass on the scale of 1g, while covering a surface area of ~ $10m^2$. Some materials and membranes explored in literature have exhibited high reflectivity, but their mass did not comply with the necessary requirements. The most promising current design is a photonic crystal, which interacts with light in a way that maximizes reflectivity and removes material by incorporating cavities into the surface, effectively reducing overall mass.

Current research into photonic crystal Lightsails primarily focuses on the reflectivity of a small segment of a flat lattice. While this is essential, the literature suggests that the full-scale structures will probably behave like traditional sails on sailboats, tending to billow. This prompts us to consider not only the problem of reflectivity on curved surfaces but also mechanical deformations and stresses within a membrane that's 1000 times thinner than a human hair.

This thesis investigates the full-scale design of the Lightsail from both the structural and electromagnetic sides. Firstly, the material, microstructure, and macrostructure of the Lightsail are analyzed to determine stresses and deformations, as well as the optimal shape for stress distribution and efficiency. Then, through topology optimization of shell elements, the main load-carrying "backbone" of the sail is identified. Secondly, optimization of unit cell photonic crystal cavities is performed across the curvature of the sail derived from the previously obtained shape, maximizing the reflectivity. Finally, the thesis proposes a design of the Lightsail that integrates all findings, which is then used to obtain a Figure of Merit value for comparison with designs in existing literature.

Contents

List of Figures

List of Tables

1

LITERATURE REVIEW

1

1.1. INTRODUCTION

Human kind has been interested in stars since the beginning of our civilization. What first began as simple gazing at the night sky full of lights evolved into weaving of stories and religious beliefs. Over the time this fascination developed into a technical understanding of the stars, using them as familiar indicators and reliable guides that provided directions to travelers both on land and at sea. Different constellations and astronomical objects today borrow their names from the aforementioned myths, such as the Orion constellation or the Andromeda Galaxy. Technical progress allowed scientists to discover the true nature of planets and stars, and calculate, with varying precision, their distances from Earth, giving a sense of reachability. As technology developed further, it brought us closer to the sky.

The invention and development of heavier-than-air, powered flight quickly contributed to human ambition in a relatively short amount of time. Since the groundbreaking performance of the Wright brothers' "The Flyer" in 1903, the technology went from a couple-second-long flight followed by unintended landing [1] to sending a man to the Moon in 1969 [2].
Since then human inventions have reached the Sun [3], several other celestial bodies [4]–[8], and even escaped the Solar System [9]. Currently, there are many missions underway to reexamine known objects more closely, such as NASA's Artemis program, [10], study new moons [11], and the collective aim of putting a human on Mars [12]–[14]. However, as their distance is measured in light-years (1 light-year = $9,46 \times 10^{12}$ km), the next step is space exploration seems out of reach - the stars.
Current technology used for space exploration is not practical for long-distance space exploration in a realistic timeline. The fastest man made object and satellite, the Parker Solar Probe [3], [15], which was developed with the aim of exploring the Sun, has now reached 150 km/s, and at its fastest and closest to the Sun it is expected to reach 192 km/s. Although the spacecraft uses several slingshot maneuvers over several years to build up its final speed, it would still need around 6600 years to reach the closest star to our Sun - Proxima Centauri [16], which is located 4.24 light years away, or $\sim 4 \times 10^{13}$ km.

Most of the current space travel methods include heavy and costly rockets, which need to haul extreme weight in fuel to escape the gravitational pull and deliver relatively small and light payloads onto orbits or other planets. For example, the now retired characteristic NASA's "Space Shuttle" weighs over 2000 tonnes just before lift-off, 1700 tonnes being fuel supplied to the main engine and boosters [17]. Apart from further developing conventional fuel propulsion, several alternative solutions have been proposed and some are in use: electric propulsion (such as resistojet, Pulsed Plasma Thrusters(PPT), Hall effect thrusters)[18], nuclear propulsion [19] or antimatter propulsion [20] (list not exhaustive). However, these examples are still not efficient for long-distance space exploration, as they are mainly limited by the their velocity, and spacecrafts utilizing such technologies would take several thousands of years to reach different solar systems. As a direct example of theoretical maximum potential of chemical propulsion , Kulkarni et al. [21] analytically showed that using the entire mass of the universe converted into chemical energy would accelerate a single proton to only 600 km/s, which would still require over 2000 years to cover the distance between Earth and Proxima Centauri.

However, many recent advancements lead to one innovative and promising solution which seems to solve both problems of weight and velocity - the light-pushed sail. It is based on radiation pressure, which is a force generated by the momentum transfer of elec-

tromagnetic radiation hitting a body and pushing the object in result [22]. The concept utilizes an ultralight sail (the object) being propelled by light (electromagnetic radiation), which accelerates the illuminated device in a passive manner, allowing the device to have a very low mass, due to not needing to carry any propellant.

The first mention of a sail-based spacecraft has been described by Tsander in 1924, when the author mentioned "working on an idea of flying using tremendous mirrors of very thin sheets" [23]. However, this note referred to solar sails. After further study and analytical description in 1950s, these were found to be inefficient for long range interstellar travel [24]. In 2010, The solar sail's effectiveness in space was successfully demonstrated by JAXA's "Interplanetary Kite-craft Accelerated by Radiation of the Sun" (IKAROS) spacecraft (visible in Figure 1.1), when the team confirmed acceleration of the spacecraft due to radiation pressure, caused by the Sun [25]. Although this technology is promising for interplanetary travel, where the distances are small compared to distances between stars, it is still insufficient for interstellar travel. The IKAROS spacecraft only reached the acceleration of 0.006 mm/s^2 [26]. As the concept of acceleration due to radiation pressure is proven, it is now a case of making it more efficient. A powerful, coherent and focused source of electromagnetic radiation could increase the radiation pressure on the illuminated sail, and a lighter, more reflective sail would be pushed to higher velocities.

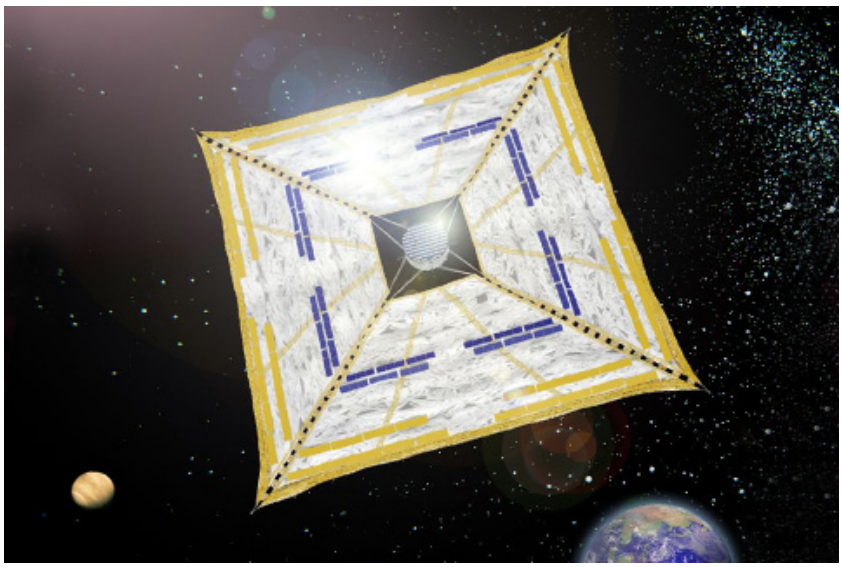

Figure 1.1: Representation of the IKAROS star sail fully deployed [27]

1.2. STARSHOT PROJECT

The Breakthrough Initiatives are a collection of space science programs established to push for technological advancement of space exploration technologies, with the aim of searching for habitable worlds and extraterrestrial life [28]. One of their programs, the "Breakthrough Starshot", is focused on developing and testing the feasibility of a nanocraft to travel to, and take close-up pictures of a promising exoplanet Proxima Centauri b, orbiting the closest star to our Sun, the Proxima Centauri, within a timeline comparable to human lifetime [29]. The predicted travel time of this nanocraft is currently estimated to be 20 years, which requires reaching velocities of 20% light speed (60000 km/s). The program

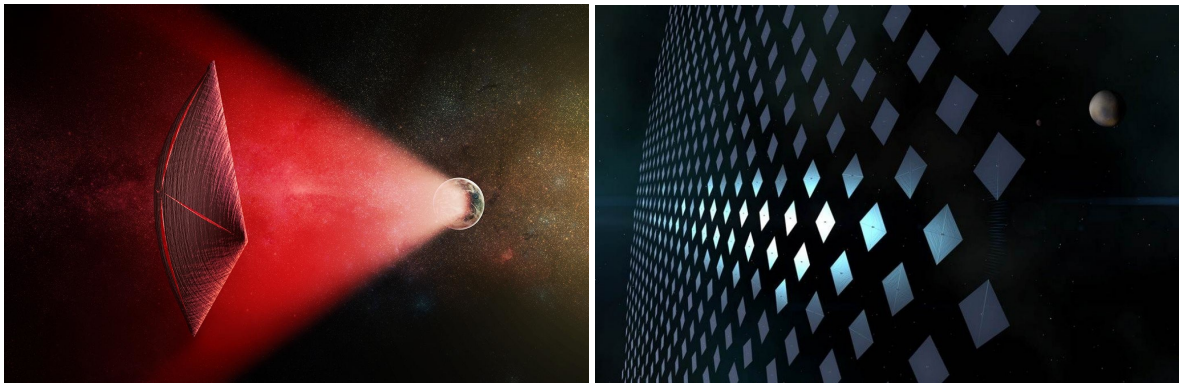

(a) (b)

Figure 1.2: (a) Representation of a laser-illuminated spacecraft, (b) Swarm of nanocrafts [32]

entails developing the light beamer (high powered laser), which would be used as the propelling mechanism, necessary instrumentation for data collection and transmission (collectively called "StarChip"), and the aforementioned sail, which would be pushed by the beamer and deliver the instruments to the destination. The ultimate aim of the program is to prove that the craft is functional and can achieve the required speeds. The next step is sending several of such devices to Proxima Centauri b to ensure successful and more complete data collection. The visual representation of the spacecraft(s) can be seen in Figure 1.2.

The Breakthrough foundation identified initial general challenges that need to be solved in order to develop a valid lightsail: heating of the sail due to high-powered laser illumination; structural integrity under rapid acceleration and deployment; and stability while riding on the laser beam [30].
From the preliminary studies by Atwater et al. [31], several design parameters have been proposed to ensure the nanocraft achieving the required velocity and fitting into the time frame of the project. The parameters are: the area of the sail suggested at 10 m^2; combined weight of the device - ~1 g; power of the ground laser 10-100 GW; wavelength of the laser at 1-1.5 μm; reflectivity of the sail needs to reach >99%; and, as mentioned by Breakthrough Initiatives, very low absorption of the materials.

As the project goes into further development and the design reaches more mature stages with many more parameters and considerations included, these initial parameters are subject to change.

The rest of this report will discuss state-of-the-art lightsail development and current solutions to each of the initial sail challenges with the aim of identifying areas where further research is needed. After analysis and literature gap identification, methods of solving the established problem will be proposed. Throughout the report, any newly found crucial research aspect will be addressed as required.

1.3. LIGHTSAIL DESIGN

The lightsail is a very novel technology being developed to cover cosmic distances at velocities that have not been attempted before. Currently there are no proven designs for such a device, thus it is crucial to recognize and understand the operating conditions to generate a successful design.
The first, and most important challenge is designing the sail's reflectivity to ensure maximum momentum transfer from the laser. In this case, reflectivity can be optimized by material properties, topology and overall shape of the sail.
In the next challenging aspect of the sail, the material and microstructure need to provide durability against heating due the high-powered laser, space radiation and other elements of the interstellar medium. The sail has to exhibit very low absorption, high heat dissipation and emissivity. This will ensure not only protection against damage due to absorbed heat, but also preservation of the sail's reflective properties in the process of increasing temperature [33]. The large radiation pressure applied by the laser will result in rapid acceleration and expose the sail to intramaterial stresses arising from forces acting on different parts of the sail. The sail not only has to withstand acceleration, but deployment and eventual deceleration, the former possibly being achieved by the use of spinning and centrifugal force, as was the case with the IKAROS spacecraft [27]. The deceleration could eventually be achieved by utilization of the star's stellar wind, however the first mission will most probably be a fly-by [34], however, the aspect of deceleration will not be taken into consideration in this thesis.
Last considerable challenge is the stability of the sail on the laser beam, navigation and very precise control. Even a minuscule course alteration at the beginning could result in significant deviation from the target at the end, assuming the sail will have no means of independent correction, due to its passive design.

The rest of section 1.3 will elaborate on these challenges and describe current proposed solutions to each of these.

1.3.1. MATERIALS

As previously mentioned in section 1.3, high reflectivity of the device is instrumental in reaching Proxima Centauri b and the most significant element influencing this overall property is a material with high refractive index (n). Due to the temperature requirements, the material also has to exhibit very low absorption properties, to mitigate any heating it might be subjected to, either from the laser propulsion or space radiation, as well as relatively high thermal emissivity, to increase the cooling rate of the sail [35]. Another consideration for choosing the right material is the changing effective wavelength acting on the sail. Due to extreme acceleration to relativistic velocity, the wavelength observed by the sail will increase over the illumination period, causing Doppler redshift. To maintain acceleration and reach the desired velocity, the material has to exhibit maximum reflectivity over a certain range of wavelengths.

Atwater et al. in their 2018 analysis [31] of the Breakthrough Starshot project argue that, taking into account the laser array's size and cost, as well as atmospheric conditions it will be subjected to, the operating wavelengths of the sail and the laser should be between $1-2\mu m$. Although there are many materials with very high refractive indexes (e.g. metals), these can also exhibit high absorption, which could lead to large, and possibly damaging, rise in temperature of the device, making them unsuitable for this project. The authors

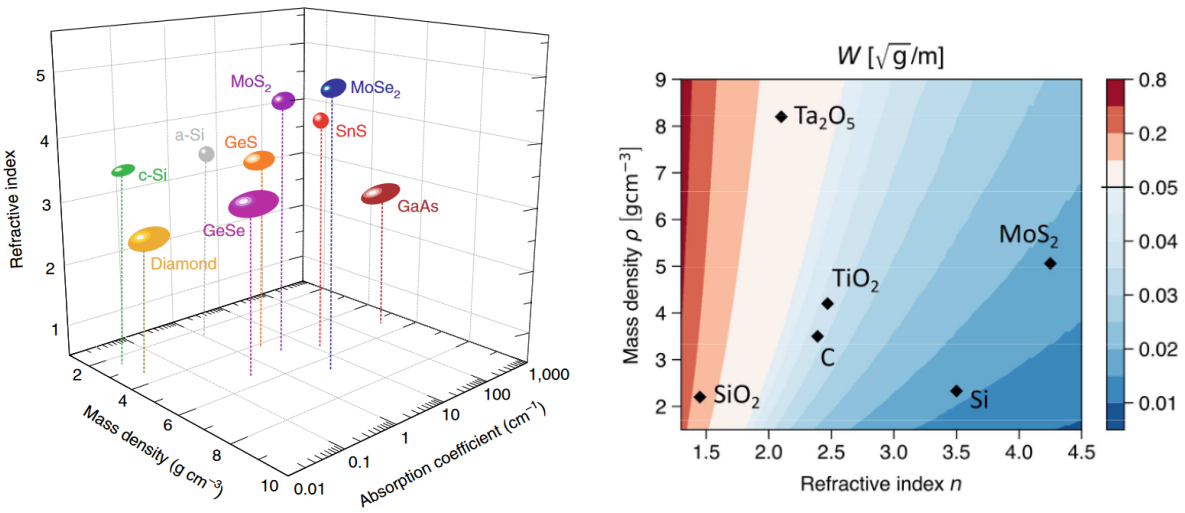

(a) (b)

Figure 1.3: (a) Relative materials comparison taking into account density, reflectivity and absorption [31], (b) Comparison of lightsail performance, mass density and refractive index [40]

propose semiconductors as promising group of materials, due to their high refractive index and low absorption. The two most promising materials presented are crystalline silicon (c-Si) and molybdenum disulfide (MoS_2), based on their balanced properties of refractive index, absorption and mass density (Figure 1.3a). Jin et al.[36] chose crystalline silicon (c-Si) in their primary study for its reflective qualities, following the material selection by Atwater et al. On top of that the authors performed optimization with silicon nitrade (Si_3N_4) as the main material, because of its favourable mechanical properties, described by Moura et al.[37]. In their lightsail study, where the authors concluded that Si_3N_4 membranes, on top of reflectivity, exhibit high intrinsic stress and high thermal noise suppression. Myilswamy et al.[38] in their lightsail stability studies chose silicon nitrade, stating its low absorption and significant Kerr nonlinearity of the material as the reasons. Tung and Davoyan [39], citing the same properties, selected Si_3N_4 and hexagonal boron nitride (hBN), both having very similar optical properties.

On the other hand, Brewer et al. [41] selected the second material mentioned by Atwater et al., MoS_2, as a promising material for lightsail purposes. The material exhibits good refractive index over a Doppler shifted range (n = 3.73 - 3.66) and virtually zero absorption in the proposed laser wavelength. Additionally, aspects that had a significant impact on material choice were good thermal emissivity of the material and manufacturability - thin MoS_2 monolayer samples have already been successfully manufactured. Furthermore, for a multi-layer design, which will be described in subsection 1.3.3 in detail, the authors applied silicon nitrade (Si_3N_4), mainly for improved thermal emissivity. It was noted that the additional material caused an increase in the refractive index, thus enhancing the efficiency of radiation pressure momentum transfer.Another study exploring the topic of reflectivity and stabilization of lightsail [42] selected Si_3N_4, highlighting ultralow absorptivity, high refractive index, robustness and scalability as the main reasons. Ilic et al. [40] focused on silica (SiO_2) and multi-layer design, with intralayer air gaps. The material choice is based on thermal emissivity considerations, as silica has low absorption and very high emissivity in the mid infrared wavelengths, but does not posses a high refractive index (n = 1.45),

compared to previously mentioned materials, like MoS_2 or Si_3N_4 ($n \sim 3-4$). Figure 1.3b compares some of the materials considered in lightsail design regarding their density ρ and refractive index n. Also focusing on multilayer design, Santi et al.[43] considered materials commonly used in optical mirrors. Although the authors considered multiple layers (1 - 7) of different materials, they concluded that titanium dioxide (TiO_2) provides the best performance in single layer structures, while additional layers of SiO_2 allow for better thermal control and increased stiffness.

Taking into account the research described above, silicon nitrade (Si_3N_4) is a primary material in lightsail research and development at this point. The material exhibits high refractive index at desired wavelengths, low absorption ($\sim 10^{-5}$ - 10^{-6}), high emissivity at the infrared, low density, and robust mechanical properties [36]–[39], [41], [42]. Moreover, it's scalable and its fabricability is thoroughly investigated [37], [41]. Lastly, the material is used in lightsail research more than any other, thus creating a larger pool of results for direct comparison and validation.

1.3.2. FIGURE OF MERIT (FOM)

While reflectivity is the main parameter responsible for efficient momentum transfer, assuming constant sail area, efforts to maximize it through multi-materials and structure design could lead to a heavier crafts. Thus, it is important to consider the mass of the device as well. To balance these considerations during design, Atwater et al. [31] proposed the use of acceleration distance (D) as the figure of merit (FOM) used for optimization. Acceleration distance is the distance required to accelerate the spacecraft to its final velocity v_f[29]. The figure can be be represented by the following equation [36]:

$$D = \frac{c^3}{2I}(\rho_l + \rho_s)\int_0^{\beta_f} d\beta \frac{h(\beta)}{R[\lambda(\beta)]} \tag{1.1}$$

where c is the speed of light; I the laser intensity;ρ_l and ρ_s the mass density of the sail and payload respectively, $h(\beta) = \beta/(1-\beta)^2\sqrt{1-\beta^2}$ is the Lorentz factor, which describes factors changing due to the device reaching relativistic speeds, with $\beta = v_f/c$. $R[\lambda(\beta)]$ is the reflectivity as a function of wavelength, which experiences a Doppler shift due to achieved velocities, represented by $\lambda(\beta) = \lambda_0\sqrt{(1+\beta)/(1-\beta)}$. Preliminary findings by Atwater et al., for $v_f = 60000 km/s$, estimate the acceleration distance to be on the scale of $D \sim 5 * 10^9$ m (Gm), considering their best-performing reflective designs [31].The FOMs in other lightsail publications are mostly comparable [31], [34], [36], [40], with some authors (where specifically stated) consider additional factors to reflect more realistic performance (e.g. temperature, described in subsection 1.3.6).

By minimizing the acceleration distance, in effect this FOM also introduces considerations of the ground-based laser, specifically its cost and size - as the acceleration distance increases, so does the diffraction-limited laser array [21], [31], [36], [40], [43]. Evidently, the FOM is a sufficient overall figure allowing for initial and direct comparison of lightsail designs.

1.3.3. SURFACE STRUCTURE

Another way of influencing the light-surface interaction and increasing reflectivity, apart from materials with high instrinsic refractive indexes, is the microstructure of the surface layer. Atwater et al.[31] simultaneously to their material study, simulated different topolo-

gies for maximized reflectivity and minimized acceleration distance regarding lightsail effectivity. They proposed and compared different designs focusing on reflectivity: single slab, multi-layer slabs (3-layer, and 5-layer), photonic crystal pillars and photonic crystal holes, all using either c-Si (the representative material in the study) or MoS_2. For the multi-layer slabs, it was assumed the intermediate layers have a unity refractive index (air).

A photonic crystal (PhC) is a material with periodic structures on a wavelength scale, with a resulting macrostructure that affects the way electromagnetic waves interact with it. By forming a photonic bandgap, which is a wavelength range that does not propagate through the material, the topology can be manipulated (size, periodicity, shape) to achieve desired optical properties, transmitting or reflecting specific wavelengths [44]. A direct comparison can be seen in Figure 1.4.

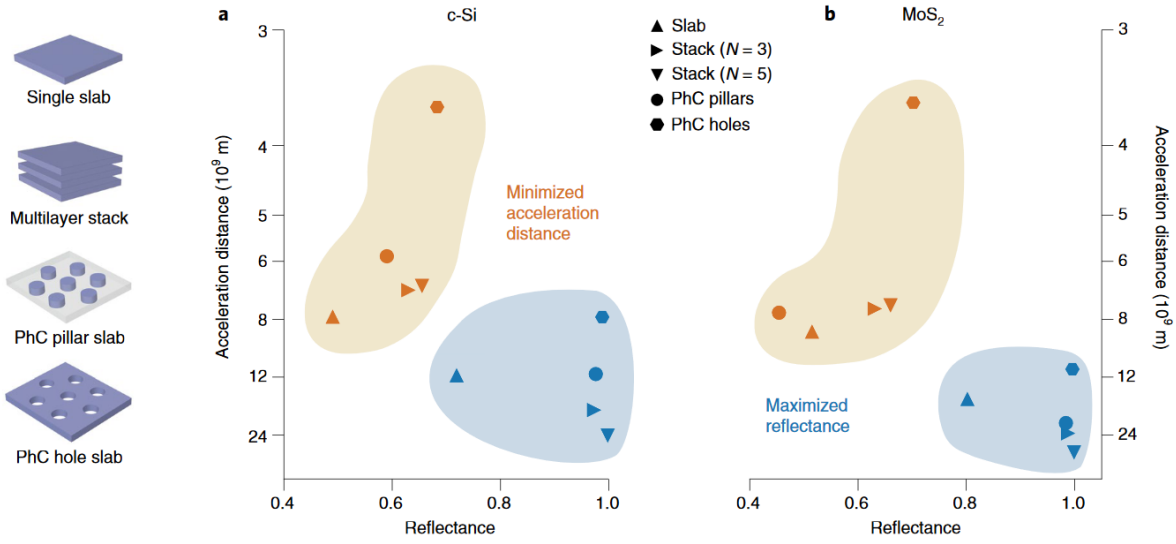

Figure 1.4: Reflective structures compared

Figure 1.4 shows that out of all studied structures, 2D photonic crystal holes exhibit a significantly superior performance over the rest of the designs when optimized for reflectivity and acceleration distance. Considering reflectance and mass, the design allowed to reach the desired velocity ($v_f = 0.2c$) in $\sim$ 150s and half the acceleration distance ($D \sim 3.5$ Gm) that any other structures achieved when optimized for reflectance.
Jin et al.[36], used inverse design and reparametrization of a photonic crystal to minimize the acceleration distance. When applied to c-Si and compared with Atwater et al. [31], they found almost a 50% increase in performance, achieving $D = 1.9$ Gm. When applied to Si_3N_4 (subsection 1.3.1), the overall optimal solution resulted in $D = 13Gm$, the increase being attributed mostly to the increase in mass density ($\rho_{c-Si} = 2.5 \text{gcm}^{-1}$ and $\rho_{Si_3N_4} = 3.2 \text{gcm}^{-1}$).
A similar approach to Jin et al. has been taken by Kudyshev et al. [45], who performed optimization by adjoint topology optimization, and variational autoencoder-assisted (VAE) topology optimization. Adjoint topology optimization utilizes adjoint sensitivity analysis, which is a mathematical technique that calculates how changing the structure (i.e. optimizing the topology) influences its performance criteria (how sensitive it is), while VAE is a neural network model used in unsupervised learning. The authors found that the op-

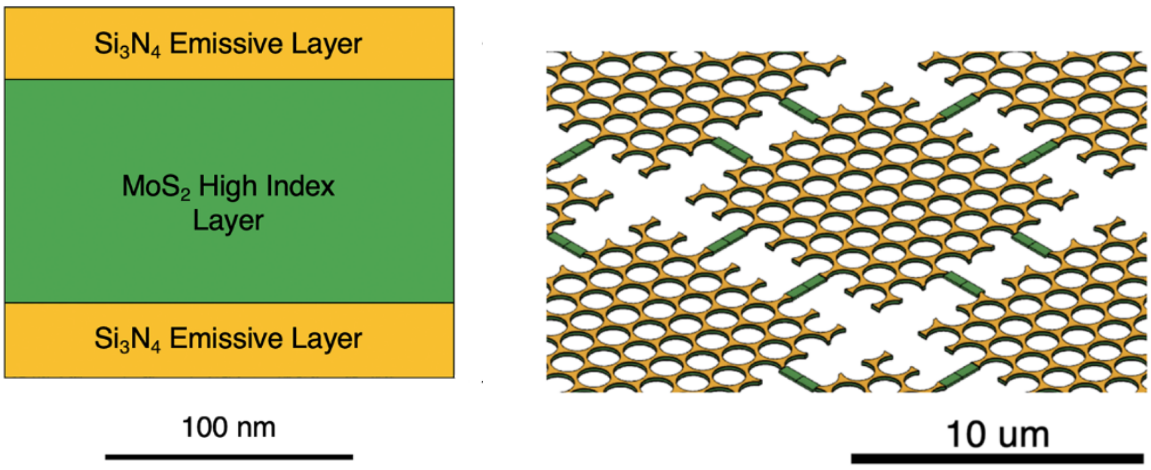

(a) (b)

Figure 1.5: (a) The layers of design, (b)The final design with Mie resonators included, connecting the reflective segments [41]

timized silicon grating achieved the same acceleration distance as Jin et al., despite the inclusion of novel methods. They, however, argue, that with the addition of more realistic constraints (stability, temperature, stresses), the variational process in the VAE could prove beneficial in such a multi-objective optimization, due to its previous efficient application in similar problems.
Brewer et al. [41] used a combination of 2D-holes photonic crystal arrangement with a multi-layer design composed of Si_3N_4 and MoS_2 (Figure 1.5a). The authors also proposed a segmented design, instead of a single sheet, with the segments being connected by Mie resonators (Figure 1.5b). The addition of this resonant structure allowed them to ultimately reach the acceleration distance value of $D = 16.7$ Gm. The design not only enhances the performance, but the segmentation would also prove beneficial during the manufacturing of the sail. Myilswamy et al.[38] also uses photonic crystals, because a nonlinear PhC exhibits a constant reflected intensity over the sail, which reduces assymetry and thus torque.

Other common designs for reflectivity and heat dissipation are based on multi-layer structures. Illic et al.[40] for their lightsail solution focus on reflective multi-layers, due to their potential of achieving high reflectivity at very low mass. The authors combine silica (SiO_2), very thermally emissive material, and silicon (Si) as the main reflective material. The authors argue that the combined refractive index and thermal emissivity make a promising solution, however the study does not provide any figure of merit relating to acceleration distance, which makes it difficult to compare to the results of other studies. Since it is a relatively early study, the authors underline that the paper only highlights the versatility and potential of multi-layer films, suggesting that future research could lead to more efficient designs.
Santi et al.[43] considered multiple materials already used in manufacture of optical mirrors, due to their reflective properties (e.g. Si, TiO_2, or MgF_2). The authors also focused on thermal management of the sail and tested different combinations of materials and varying amount of layers. However they concluded that only a single layer of TiO_2 achieved the best result in terms of efficiency, while a multi-layer design only added some benefit of thermal

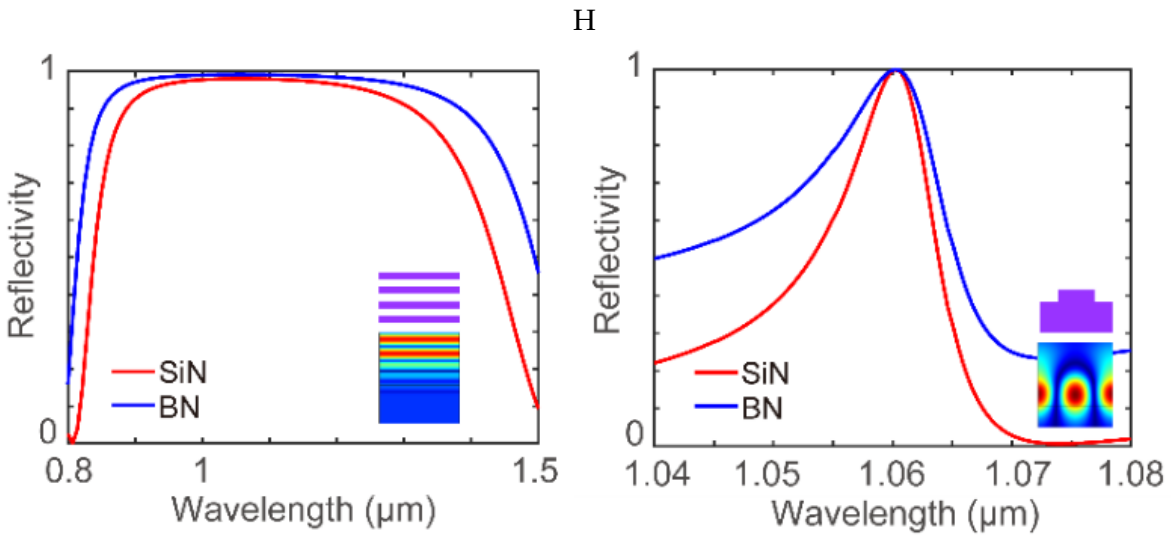

Figure 1.6: Graphs showing unity reflectivity spectrum for both a Bragg reflector (left) and a GMR reflector (right) [39]

emissivity.
Although not parametrized nor optimized for interstellar travel, but focusing on interplanetary distances, Tung and Davoyan[39] studied the efficiency of a lightsail. They considered both layers (Bragg reflector) and a guided mode resonance (GMR) reflector (periodic structure/grating), for which they used first a stoichiometric silicon nitride (Si_3N_4), and then hexagonal boron nitride (hBN). The reflectivity was optimized for laser wavelength $\lambda = 1.06\ \mu$ m. Authors found that both techniques are promising for efficient space exploration, however, the multi-layers design exhibits a smaller absorption coefficient ($\alpha \sim 10^{-6}$) and a broader reflectivity spectrum (Figure 1.6). As evident from Figure 1.6, the GMR reflector has a much thinner reflectance bandwidth, but on the other hand, the design allows for much thinner structures, compared to the Bragg reflector.

Evidently, single-layer 2D photonic crystal structures exhibit better performance over other mentioned designs, considering reflectivity and acceleration length. This design, considering its design parameters (shape, size, alignment) could allow for degrees of freedom during precise optimization. However, an additional layer of a highly emissive material, as presented by Brewer et al. [41] might prove beneficial when considering thermal management.

1.3.4. SIMULATION METHODS

There are three main methods of simulating the metasurface-electromagnetic wave interaction: Finite Element Method (FEM), Finite Difference Time Domain (FDTD), and Rigorous Coupled Wave Analysis (RCWA) [46]. All methods solve Maxwell's equations - a set of fundamental equations describing the propagation and interaction of electric and magnetic fields. FDTD operates in the time domain, and RCWA and FEM are frequency-domain techniques. The following is a list containing short descriptions and highlighting the main differences between the above methods:

RCWA is a semi-analytical method that works by decomposing a structure into layers, calculating the interaction of light with each layer, which are then combined together in a scattering matrix which is then used to extract values like reflection and transmission [47].

FDTD works on a mesh grid, where the magnetic and electric fields are calculated at each grid point and then updated after each time step to get the overall image of the fields over time [47].

FEM discretizes the computational domain into small elements and approximates the required values, in this case, electric and magnetic fields, in each of them [48].

Paulsen et al. [46] compared all of the above methods on the same metagrating structure, and found that all of the methods have similar simulation results, although they differ significantly in computational time. The FEM and FDTD methods were implemented through proprietary software (COMSOL Multiphysics® and FDTD Solutions by Lumerical Solutions, Inc., respectively), while RCWA was implemented in-house through Matlab®. RCWA was found to be the fastest and best suited for transmission and reflection computation, while FEM was found to be the slowest, mainly due to each field having to be calculated to analyze single results. Yet, the software packages for FEM and FDTD allow for good customization through their dedicated toolboxes, their user interfaces enable intuitive control and manuals ensure a comfortable introduction. RCWA as an in-house solution requires extensive knowledge of algebraic computations and is non-trivial to implement.

Table 1.1: Comparison of simulation times for different methods and outputs [46]

Method	Transmission spectrum	Single wavelength field	Full spectrum and field
FEM	13 min 11s	6 s	13 min 11 s
FDTD	1 min 7s	59 s	5 min 4 s
RCWA	18 s	12	7 min 10 s

1.3.5. NOVEL DESIGN PROCESS THROUGH TOPOLOGY OPTIMIZATION AND MACHINE LEARNING

Current realistic design includes reflectivity, heating, stresses, stability, and mass considerations. Although general designs have been proposed, with photonic crystal structure being most promising at this stage (described in subsection 1.3.3), most attempts only take into account the periodic round hole diameter and pitch, or several layers of different materials, optimizing for maximum reflectivity of a unit cell with orthogonal incidence angle. To explore the possibility of more novel designs of PhC unit cells Norder [49] implemented convolutional neural network (CNN), following lightsail optimization by Jin et al. [36] by the method of moving asymptotes (MMA)(Figure 1.7a), and convolutional neural network implementation for topology optimization (CNN-TO) introduced by Hoyer et al. [50] intending to optimize a unit cell shape for maximum reflectivity of a specific laser wavelength range. Topology optimization is an engineering design method that introduces a novel methodology to the design of structures with respect to pre-set requirements. By utilizing iterative analysis and advanced algorithms it reaches optimal structural material

1

distribution within a given space, most often resulting in non-intuitive designs. Because of this, the traditional experimental approach, which often relies on preconceived designs of structures that are under similar boundary conditions and loads, is eliminated. As a result, it saves time, creates novel designs, and converges at solutions that not only have the best performance but also use the least amount of material. Nevertheless, it is most commonly used in conjunction with engineering intuition and established design principles. This ensures that the design is not only comprised of the raw, best parameters coming out of the optimizer but also follows design standards and practical considerations. MMA is an iterative process that dynamically adjusts initial variables based on calculated gradients from the previous iteration, guiding the search toward the optimal solution. CNN is a type of machine learning (ML) model that can be used in topology optimization by utilizing its image-processing functionality. Both methods of optimization converged to the same design Figure 1.7b, however, the CNN-TO reached the design in fewer iterations with a smaller average acceleration distance. Moreover, the CNN-TO method resulted in non-intuitive designs for high-dimensional design problems, highlighting its potential for more efficient designs.

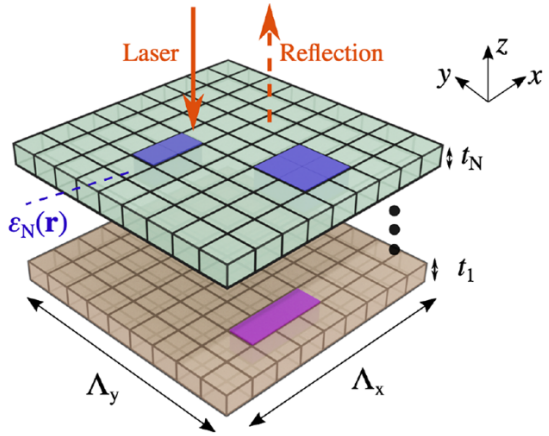

(a)

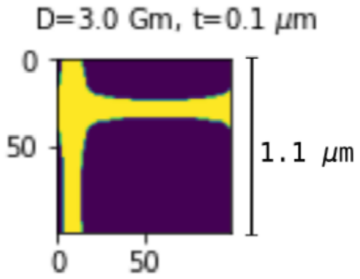

(b)

Method	$\overset{*}{D}[10^9 m]$	$\bar{D}[10^9 m]$	$\bar{it}[-]$
CNN-TO	3.0	3.8 ± 1.3	1047 ± 645
MMA-TO	3.0	4.4 ± 1.6	1328 ± 760

(c)

Figure 1.7: (a) Lightsail optimization method schematic by Jin et al. [36], (b) Best unit cell design, and (c) comparison of both optimization methods, using best result acceleration distance $\overset{*}{D}$, average acceleration distance result $\bar{D}$, and mean number of optimization iterations $\bar{it}$[49]

1.3.6. THERMAL MANAGEMENT

Due to the high powered ground-laser illuminating the lightsail, the device will not only accelerate due to momentum transfer of the photons, but also inevitably absorb some of the laser's energy as heat. This will lead to a rise in temperature of the lightsail, resulting in changing material properties. Depending on the change in temperature, the device's efficiency could diminish, or even melt the sail. The vacuum of space allows radiation as the only method of effective cooling. Only a couple of studies considered the thermal management of the lightsail and discussed the possible solutions in this environment. Atwater et al. [31] argue that the material's emissivity (ϵ) cannot be lower than $\epsilon = 10^{-3}$, as it would most likely lead to insufficient heat radiating out of the device, and that resonant structures should be avoided, as they can lead to an increase in absolute absorptivity. The latter has

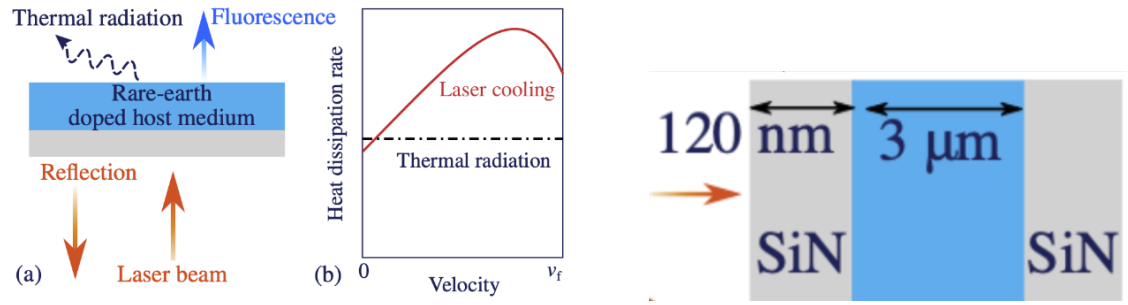

(a) The concept setup

(b) The lightsail's layers

Figure 1.8: Concept proposed by Jin et al. [51]

been observed by Tung and Danovan [39], who compared Bragg reflectors to GMR reflectors. Although both structures were able to achieve near unity reflectivity, the GMR's resonant interaction with light resulted in an absorption coefficient $\alpha_{GMR} \sim 10^{-4}$, a two orders of magnitude difference relative to the Bragg reflector, $\alpha_{Bragg} \sim 10^{-6}$. For heat emission purposes, most studies propose the multi-layer (Bragg reflector) approach, which assumes a core material as the main reflective layer with very high refractive index, and a thin layer of a highly emissive material on the outside to absorb the core layer's heat through conduction, and radiate it out into space. Ilic et al. [40] approached this problem putting silica (SiO_2) as the emissive layer on top of silicon (Si). Although they tested for several layers, they found that a simple two-layer design proved to achieve most benefit, balancing between reflectivity, emissivity and production complexity. Similar conclusion was achieved by Santi et al. [43] who considered multiple layers with combinations of different materials, however found that a single core layer of reflective material TiO_2 performs better in terms of momentum transfer, while the addition of emissive SiO_2 provides enhanced thermal management. Brewer et al. [41] combined PhC design with multi-layers, choosing MoS_2 as the core material and Si_3N_4 for the emissive layers on both sides of the inner layer. The silicon nitrade layer slightly contributed to overall reflectivity, and resulted in an improved performance. Although the initial design reached values of $D = 10.6$ Gm, before the added thermal constraints, which impaired the maximum acceleration, resulting in $D_{withT} = 23.3$ Gm. Jin et al. [51] utilized the effect of solid-state laser cooling and anti-Stokes fluorescence for thermal management based on rare-earth materials. The phenomenon entails light emitting at higher frequency, than the frequency of the absorbed laser [52]. Concept and the lightsail setup can be seen in Figure 1.8, with the emissive layer placed in the center, composed of Ytterbium (III)-doped Yttrium Lithum Fluoride (Yb^{+3}-doped YLF) , and the reflective layers of SiN being present as the outside layers. The authors simulated much heavier devices ($\sim$ 1kg) and much lower speeds ($0.01c - 0.05c$) than suggested by Breakthrough Starshot. However, it is suggested that higher speeds are achievable with a variant frequency laser or using rare-earth ions spanning a wider wavelength, as the Doppler shift becomes a significant challenge.

1.3.7. BEAM RIDING STABILITY

The last design consideration mentioned in section 1.2 is the stability of the sail on beam. In previous sections materials and topology of the surface were only considered for maximum reflectivity of a unit cell. However, taking into account the large scale of the sail and its

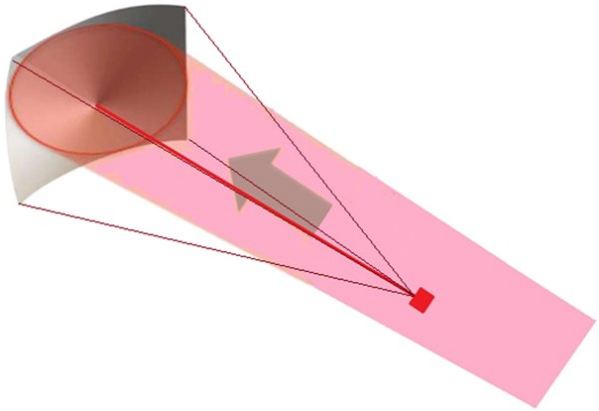

Figure 1.9: Schematic illustration [53].

interaction with the entire laser beam, reflectivity over the entire sail must be considered. If the center of the beam is not properly aligned with the center of the sail, introducing a very slight deviation from the calculated path in the acceleration stage, resulting in a large offset from the final goal, or the sail being entirely expelled from the beam. Since the entire device will most likely be passive (i.e. does not carry any independent propulsion or trajectory correcting system) the stabilizing elements have to be incorporated either into the sail's shape and topology, or to the beam.

Considering the shape and weight distribution of the entire device, Popova et al. [53] conducted mathematical analysis using equations of motion for different sail shapes - flat, spherical and conical. The assumed setup of the sail resembles a parachute, with a billowing sail, tethers and the StarChip being dragged behind (Figure 1.9). The authors argue that such a setup does not require spinning of the device to ensure stability, unlike the design that incorporates the chip directly in the sail. With a flat laser beam profile, the conical and spherical lightsail remain stabilized as long as the distance between the chip and the sail (L) is larger than the sail's radius of curvature (R). A relation of $L > 2R$ is required for a Gaussian distribution to stabilize the sails without spinning. The authors found that a flat sail is unstable in every case. However this setup would require an additional incorporated stiffening system or a frame to prevent the membrane with tethers from collapsing in on itself.

On the other hand, Manchester and Loeb [54] show that a conical shape on a Gaussian beam is not stable without additional control or sufficiently high spin frequency, and that only spherical shape is viable for self-stabilizing purposes. Moreover, the authors point out that a spherically shaped sail provides advantages over conical shape in terms of manufacture, storage and deployment, among others.

Gao et al. [55] through mesh-based time-domain simulations argue that a smooth sail, no matter the shape (flat, spherical or conical) will collapse on itself when accelerated by a Gaussian beam without sufficient spin. Moreover, when subjected to a small perturbation it will immediately get ejected from the beam and veer off course. Paraboloid sails with sufficient spin prevent collapse and ensure the sail stays on the beam after introduction of small perturbations. However, the shape curves and elongates throughout simulation's duration (1s) enough to introduce internal reflections which act on opposite ends of the sail, imparting destabilizing forces (Figure 1.10b). Although flat sails with metagrating have been successfully simulated to be stable, the used parameters all fall below the initial

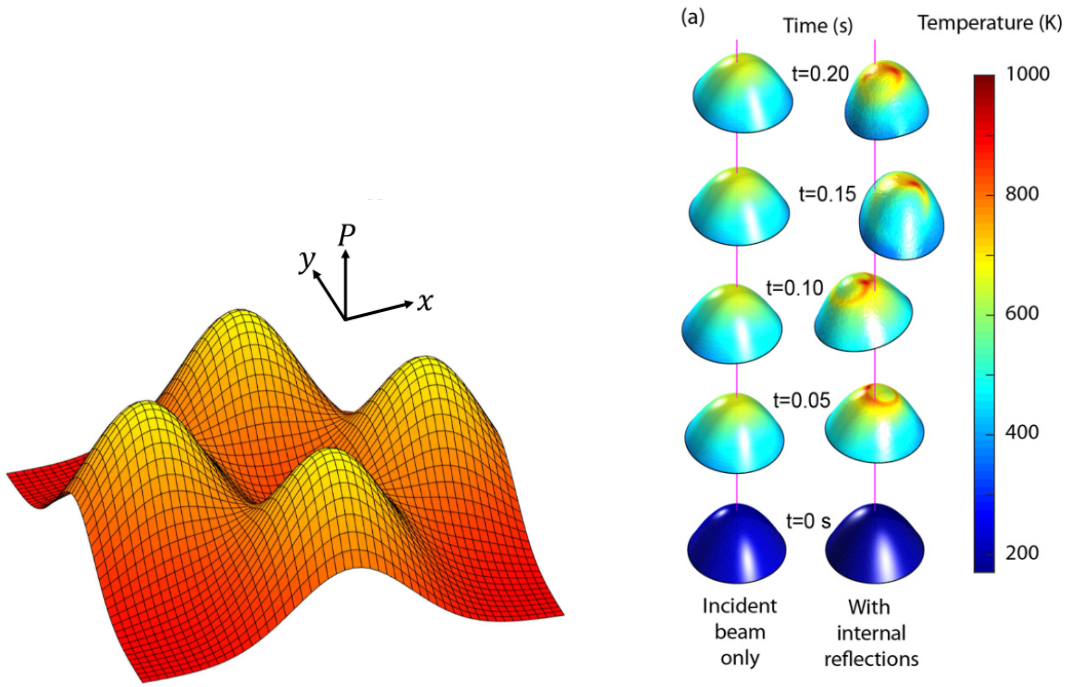

(a) Gaussian beams profile [54]

(b) Paraboloid shape without and with internal reflections [55]

Figure 1.10: Stability methods

Breakthrough Starshot targets.

Topology manipulation is mentioned by Siegel et al. [56], who propose the use of metasurfaces with grating-like structures on top to control the light-surface interaction and design for self-stabilizing behavior. The metasurface deflects the laser beam in a normal direction when the lightsail is positioned perpendicularly to the beam. At the moment of deviation from the center of the beam, or/and at a skewed angle, the metasurface deflects light in such a way as to create resultant forces pushing the sail into the initial position, stabilizing the device. The authors tested different grating designs and concluded that they determined a large range of parameters exhibiting self-stabilizing behavior. A similar design has been proposed by Ilic et al. [57], whose findings corroborate the structure's ability to exhibit self-stabilizing behavior. A representation of the process and potential structures can be seen in Figure 1.11. Salary and Mosallaei [58] in their lightsail optimization focused on finding the balance between acceleration and beam riding stability throughout the entire Doppler-shifted spectrum. Authors report that using the meta-grating nanostructures, the simulated device reached desired velocity in 485s and stayed within the beam diameter. Gao et al. ([55]) simulated a spinning flat sail with metagrating applied which stayed marginally stable on the beam throughout a 5s simulation, after being put in an offset position initially. A different concept was applied by Myilswamy et al. [38], who focused on achieving stability by manipulating the reflected intensity, instead of the direction. The authors created a guided mode resonance of a silicon nitride photonic crystal for this purpose, and thus mitigated any uneven forces acting on the sail, resulting in a stable design. Rafat et al. [59] proposed a solution for stability by damping the internal degrees of freedom of the sail, and thus the vibrations.

In addition to sail design, Manchester and Loeb [54] ensured stability by strategic im-

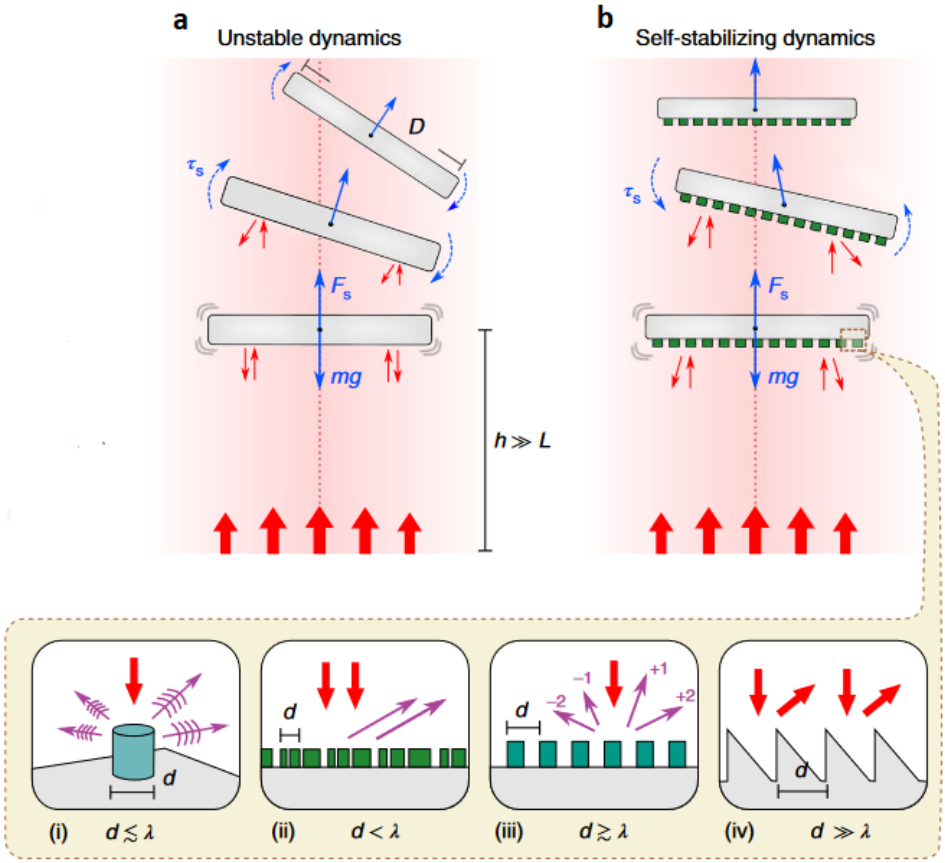

Figure 1.11: Comparison of stabilizing behaviors of (a) a smooth plate and (b) a plate with metasurface, as well as light-structure interaction of varying gratings [57]. L - aperture size, D - object diameter, d - grating pitch, λ - wavelength

plementation of multiple off-center laser beams. The positioning of these lasers generates a distinct beam profile, resulting in a basket-like dip, as visible in Figure 1.10a. This maintains the sail's stability by exerting a corrective force on the sail's surface that deviates from its central position.

1.3.8. STRESS CONSIDERATION

Most of the research on Lightsails has been focused on achieving the highest possible reflectivity, considering materials and structure (subsection 1.3.1, subsection 1.3.3), followed by heating (subsection 1.3.6) and stability (subsection 1.3.7). The mentioned figures of merit (FOMs) (subsection 1.3.2) mostly entail reflectivity, as well as mass, and minimizing the distance leads to minimization of laser-array size and cost, which has to be adjusted to account for diffraction and power required [21], [31], [34], [36], [40]. Some authors additionally consider heating aspects to create a more realistic predicted performance. However, the aspect of stress analysis in such structures is largely underexplored. While certain sources analyze the stresses induced by radiation pressure [60], they focus on solar radiation pressure utilized in solar sails, which is much lower compared to the pressure exerted by high-powered lasers. This ultimately leads to vastly different design considerations.

The fundamental aspect to consider during stress analysis is the overall shape of the

lightsail. There is very limited literature addressing this specific topic, mostly coming from stability analysis [53]–[55], but the resulting design is usually reminiscent of a boat sail. To my knowledge, only one article analyzed the theory, proposed a general design, and performed stress analysis regarding the lightsail application. Campbell et al., [61] performed a thorough analysis and suggested that lightsail designs must be significantly curved (must billow) when taking into account heating, stability, stresses, and eventual tearing and crack propagation. A visual representation (with an exaggerated sail curve, for demonstrative purposes) can be seen in Figure 1.12.

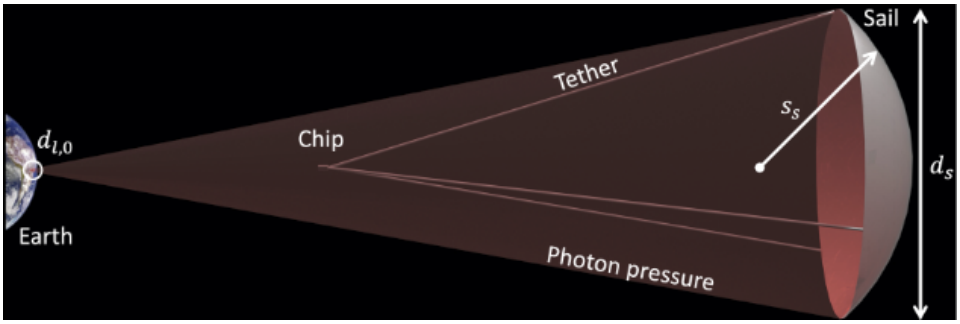

Figure 1.12: Representation of the Starshot device, with a visibly billowing sail [61]

Although the authors assumed a uniform laser profile (flat, "top hat"), their stress analysis provides a reliable, simplified prediction. The authors state that an unbent surface will oppose the radiation pressure due to ground-laser irradiance by its bending stiffness, resulting in stress $\sigma_{flat} = \frac{Pd_s^2}{t_f^2}$, however a curved profile results in $\sigma_{curved} \sim \frac{Ps_a}{t_f}$, where P is photon pressure, d_s is the sail diameter, s_s is the radius of curvature, and t_f is the sail film thickness. Thus, the lower the value of s_s, the lower the stress value. However, since the actual curvature was assumed to be comparable to diameter ($d_s \sim s_s$), the ratio of the stresses can be estimated as $\frac{\sigma_{flat}}{\sigma_{curved}} \sim \frac{d_s}{t_f}$. With scales of $t_f \sim 100$ nm and $d_s \sim 1$m, evidently the curved shape immediately provides a significant advantage over a flat shape in terms of minimizing stresses. Apart from acceleration length (L), which follows the same formula as Ilic et al. [40] and Atwater et al. (2018) [31], with a modification of varying laser power, the authors introduced a figure of merit ($\mathscr{F}$) which expands on the original acceleration length L by adding stress, strain and temperature considerations. Selected results from the analysis can be seen in Figure 1.13.

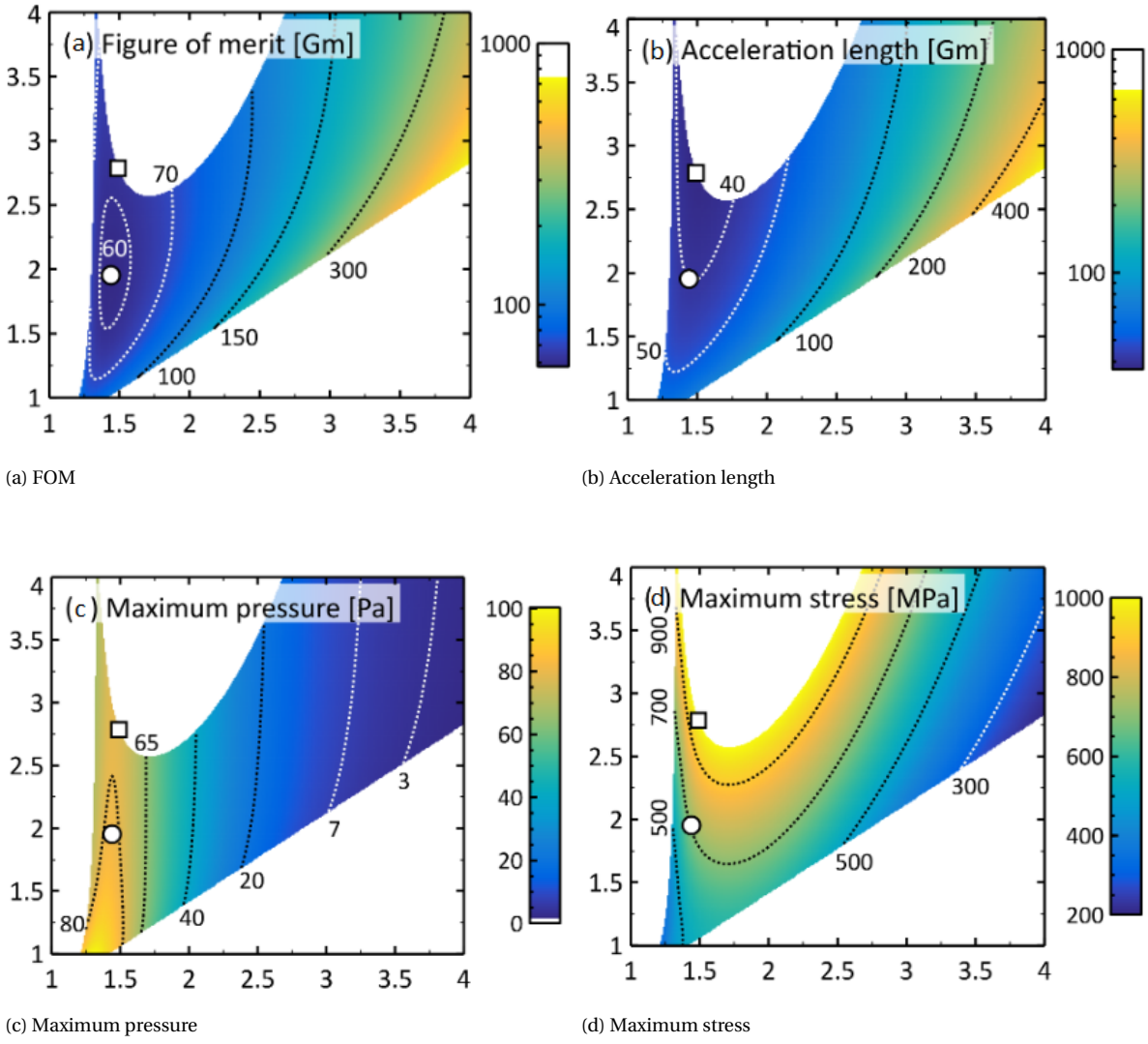

(a) FOM

(b) Acceleration length

(c) Maximum pressure

(d) Maximum stress

Figure 1.13: Excerpt from the figures produced by Campbell et al. [61]. The large white spaces indicate the designs that were removed due to several considerations, such as multiple reflections increasing heating in the center, too high temperatures (> 1000 K) or too large stresses (σ > 1000 MPa). The white circles indicate the designs with lowest FOM, whereas the white squares indicate the lowest acceleration length L design

1.4. SUMMARY AND CONCLUSIONS

A goal of reaching Proxima Centauri in a span of 20 years from launch has been set by the Breakthrough Initiatives. The most promising and suggested project capable of achieving the required speed of 60000 km/h and reaching the planet orbiting the star, Proxima Centauri b, is the lightsail. This design utilizes the force generated by a high-powered ground laser to quickly be propelled to relativistic speeds, allowing it to traverse a distance of 4.22 light years in such a short time.
Initial research into materials and design, focused on minimizing the acceleration distance, of the sail, (being the figure of merit (FOM)), was conducted, with new and more complex developments being published at an increased frequency.
Following from previous sections it's evident that progress in lightsail research requires more realistic figures of merit and simulations to move closer to the ultimate goal of sending the satellites to Proxima Centauri b. More complicated FOMs change the performance and design considerably. Because the operational environment and the requirements are complex, yet the entire device is delicate, it is important to maximize its performance while retaining integrity over the entire duration of operation, mainly during its acceleration phase.
The analyzed literature presents many distinct designs and suggests optimal materials, with performance potentially allowing to fit within the presented time frame. However, the presented designs are mostly limited to unit cell topology, to maximize the reflectivity of an infinite photonic crystal. Many new findings are re-using known designs with small increases in complexity to achieve the goal, simulating an increasingly realistic environment and as a result increasing the acceleration distance.
In most studies, for simplicity, it is assumed that the optimized unit cell design has been applied to the entire area of a flat sail. Intra-material and -structure stresses resulting from applied pressure (although included in one article by Campbell et al. [61] as "maximum value allowed") have not been considered in the design of the sail in its entirety. The topology has been optimized for reflectivity and its shape is considered for stability, with material(s) thickness considered for thermal management.
When the above-mentioned parameters are considered on the macro scale, together with interactions between unit cells, the sail profile might change considerably. This could result in a sail of varying unit cell design to account for varying properties over the entire area. Only one publication performed stress analysis on a simple, homogeneous spherical sail, with perfect mirror assumption. The literature shows that the photonic cavity topology is one of the most promising candidates, mainly due to its high adjustability in terms of wavelength reflectivity and inherent lesser weight (due to material removal). Thus it is important to approach the lightsail design from both sides at the same time, considering structural integrity as well as its reflective properties.

Therefore, taking into account existing and often applied materials and key performance indicators, the structural and electromagnetic analysis of the Lightsail will be performed based on its operating conditions and behavior. Initially, the stress distribution will be examined, followed by an evaluation of its reflectivity and efficiency in harnessing the laser's momentum, ultimately leading to a design integrating the findings.

2

METHODS

For reasons described in subsection 1.3.4, COMSOL Multiphysics® software will be used to perform all of the simulations unless otherwise stated. It was chosen due to its easy environment with a user-friendly interface, proven metagrating-EM simulation capabilities, and availability. Moreover, it allows for comfortable computer-aided design (CAD) at both macro and micro scales with minimal algorithmic expertise, and its post-processing toolbox allows for quick result analysis, visualization, and data export for more in-depth understanding and clearer presentation using such software as Matlab®.

2.1. STRUCTURAL ANALYSIS

In this section, the structural analysis of the Lightsail is performed. First, initial values suggested by the literature are reviewed. Then, the effective material parameters are extracted from photonic crystal patterned plates. A model established in literature is reproduced to validate the model used in further analysis. Lastly, the setup of the model is described and presented.

Several key assumptions were made, following guidelines from available literature ([53]–[55], [57], [59], [61]), to simplify the structural analysis performed and ensure its feasibility. Although we believe they provide a sufficient approximation, given the current Lightsail research status, their outline is crucial for understanding the limitations and scope of this thesis. These are: uniformly distributed, constant force acting on the sail resulting from a "tophat" laser beam shape; smooth, homogenized surface (no stress concentration between circular cavities); linear behavior (nonlinear where mentioned); no absorption, thus no stresses arising from thermal expansion; neglected momentum loss through sail's thermal photon emission; neglected interaction of the sail with the interstellar medium [62].

2.1.1. PRELIMINARY STARSHOT DESIGN AND VALUES OUTLINE

To simulate the basic plate, we follow the initial suggested values in [31], with LPCVD silicon nitride as the material [63]:

Table 2.1: Initial values parameter values outlined in [31] and [63]

Parameter	Symbol	Value
Area	A	$\sim 10\text{m}^2$ (Radius $\approx 1.784\ \text{m}^2$)
Thickness	t	~ 100 nm
Laser irradiance	I	$10\ \text{GW/m}^2$
Pressure (due to the laser)	P	≈ 66.7 Pa
Wavelength	λ	1550 nm
Density	ρ	$3000\ \text{kg/m}^3$
Young's Modulus	E	290 GPa
Poisson's Ratio	ν	0.27

The initial unit cell design was taken to be: lattice constant $a = 1000$nm and circular cavity radius $r = 450$nm, being the approximate values of Norder's [49] optimized unit cell (described in subsection 1.3.5). Because the Breakthrough Starshot initiative is still in its early stages, no specific wavelength has been chosen as the definitive choice for this application. However, wavelength $\lambda = 1550$nm is one of the preferred wavelengths in free space

optical (FSO) communication (a term used for outdoor wireless optical communication) due to low attenuation, high component availability, and high data rate transfer. These lasers are also 50 times more powerful than other preferred, but shorter wavelength lasers, for example, $\lambda = 850$nm [64]. As it seems to be the most viable candidate to be used in the Breakthrough Starshot project, it is chosen as the operating wavelength for the rest of this work.

2.1.2. OBTAINING EFFECTIVE PROPERTIES FOR HOMOGENIZED PHC PLATES

The simplest way to effectively perform structural analysis on a lightsail would be to create the 3D model, apply boundary conditions and stresses and analyze the results. However, modeling a meter-scale lightsail with micrometer-scale photonic crystal cavities would require immense computational power, which is not realistic. Instead, it is possible to approximate the effective properties of such a structure by modeling a small portion of it. A small version of the plate with real-size PhC cavities was modeled in the software and compared to the analytical approach laid down by Timoshenko and Woinowsky-Krieger [65] applicable to round flat plates with clamped edges:

$$D = \frac{Et^3}{12(1-\nu^2)} \tag{2.1}$$

$$\delta_{max} = \frac{pr^4}{64D} \tag{2.2}$$

where D symbolizes flexural rigidity, E Young's modulus, t thickness, ν Poisson's ratio, δ_{max} maximum displacement, p intensity of the uniformly distributed load, r the radius of the circular plate. Combining equations Equation 2.1 and Equation 2.2, we obtain the formula for the Young's Modulus of the material used:

$$E = \frac{pr^4 \times 12(1-\nu^2)}{64\delta_{max}t^3} \tag{2.3}$$

Smaller, flat plates ranging from $r = 5$ μm to $r = 50$ μm were simulated to obtain effective Young's modulus E_{eff}. The edges were fixed and uniformly distributed pressure $P = 66.7$Pa applied. The used lattice constant $a = 1\mu$m and circular cavity radius $r = 0.45\mu$m remained the same, only the overall radius was changed. The entirety of simulated sizes, as well as the respective effective values obtained, can be seen in Table 2.2, and their geometry is presented in Figure 2.1.

Evidently, the E_{eff} goes down with increasing radius of the structure, however the change between each subsequent value seems to be decreasing in comparison to the preceding one, suggesting a convergence point. More simulations could help closer determine the converged value, however, due to computational limitations it is impractical to perform further studies in the permitted time frame.

Table 2.2: The effective Young's modulus of PhC circular plates at various radii

Radius [μm]	E_{eff} [GPa]
5	192.68
10	184.52
15	162.41
25	154.37
35	152.15
50	149.11

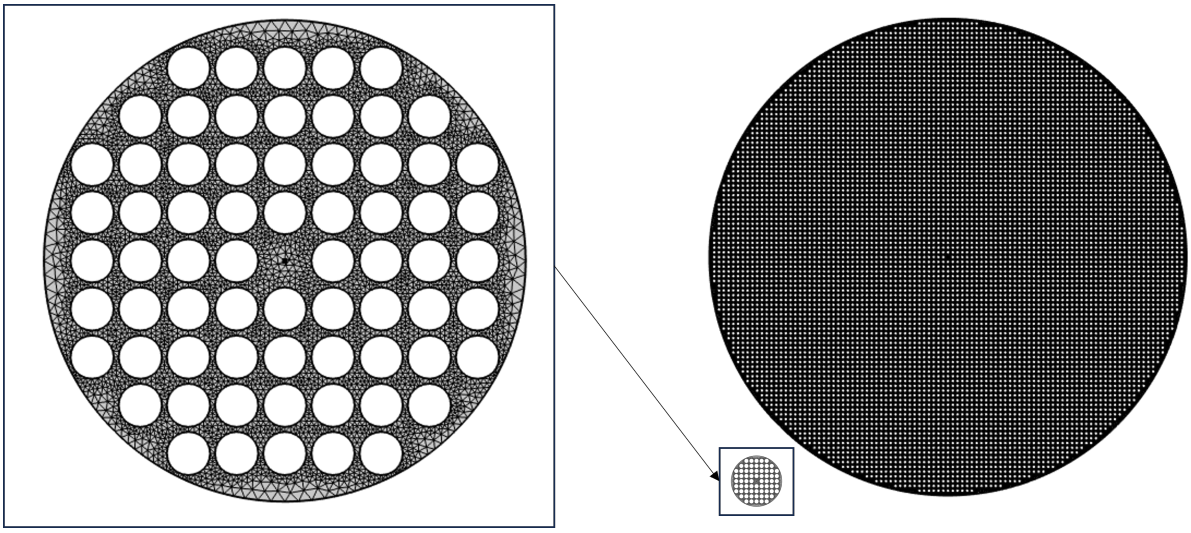

Figure 2.1: R = 5 μm (left) and R = 50 μm (right) models compared

Thus, following the values, E_{eff} = 130 GPa was agreed upon as the homogenized parameter for use in large-scale simulation, which adequately approximates the effective parameter for this study. By simple mass simulation of a solid plate compared to a PhC plate, the homogenized density was obtained, amounting to ρ_{PhC} = 1092 kg/m^3. The Poisson's ratio value is assumed to stay the same at ν = 0.27.

To summarize, the effective values obtained are as follows:

$$E_{eff} = 130GPa \quad \rho_{PhC} = 1092kg/m^3 \quad \nu = 0.27 \tag{2.4}$$

2.1.3. FOUNDATIONAL STUDY REPRODUCTION AND STRUCTURAL ANALYSIS MODEL VALIDATION

The main structural basis for this work is the design proposed by Campbell et al. [61]. Moreover, the reproduction of their model serves as a validation study for the model used for the rest of this dissertation. Thorough argumentation is presented in subsection 1.3.8.
The design can be modeled as a thin spherically curved plate that distributes stresses similarly to a sail billowing under wind pressure. All calculations and simulated values were based on the numerical calculations outlined in the referenced article and entered by hand, ensuring consistency in applied forces.
The main result of comparison in the majority of articles dealing with the lightsail, the so-

called Figure of Merit (FOM)(subsection 1.3.2), is the acceleration distance D, which here is augmented by variable laser power, and takes the form of:

$$D = \frac{m_{tot}c^3}{2}\int_0^{\beta_{max}} \frac{\beta\gamma}{\rho_{avg}\phi(1-\beta)^2}\,d\beta \tag{2.5}$$

where m_{tot} is the total mass, β the lightsail velocity to light speed ratio (here $\beta_{max} = 0.2$), $\gamma = \frac{1}{\sqrt{1-\beta^2}}$ is the Lorentz factor, ρ_{avg} the average reflectivity, and ϕ is the laser power.
The pressure used in stress calculation follows the equation used by Campbell et al. for pressure at the center of the sail at time = 0s [61]:

$$P = \frac{8\rho_{\perp}\phi}{\pi c d_s^2} \tag{2.6}$$

where $\rho_{\perp}$ is the perpendicular reflectivity of the material, ϕ[W] laser power,c[m/s] speed of light, d_s the diameter.
The comparison between selected values is presented in Table 2.3, where σ_{center} is stress at the center, δ_{center} the deflection at the center, P the pressure applied, D the acceleration distance, and t_l the laser-on time. It can be noticed the discrepancies between comparable values are minimal, and any differences are related to approximations that were made necessarily. Thus the replicated environment is reliable enough to perform further simulations.

Table 2.3: Comparison of reproduced results [61] at $t = 0s$.

	σ_{center} [MPa]	δ_{center} [m]	P[Pa]	D [Gm]	t_l [min]
Simulated	666.0	0.0577	82.55	38.376	17.66
Campbell et al.	~ 660.0	-	~ 82.5	38.7	17.4

Next, a curved sail with initial Starshot and homogenized PhC silicon nitride values was created for direct material comparison. The radius of curvature ($s_s = 4.15$m) was chosen to maintain the same diameter-curvature ratio as Campbell et al.'s design: $\frac{d_s}{s_s} = 0.85965$, while keeping the diameter at $d_s = 3.568$m, as at this point the level of acceleration distance is impacted by the curvature.

Table 2.4: Values used in [61] and values used in this study

Parameters	**Symbol**	**Campbell et al. (2022)**	**Simulated (SiN PhC)**
Laser power	ϕ	30GW	30GW
Diameter	d_s	1.47m	3.568m
Radius of curvature	s_s	1.71m	4.15m
Film thickness	t	105.9nm	100nm
Young's Modulus	E	21.8GPa	130GPa
Density	ρ	5060kg/m^3	1092kg/m^3
Poisson's ratio	ν	0.24	0.27
Perpendicular refl.	$\rho_{\beta,\perp}$	~ 0.70	~ 1

The resulting values are presented and compared in Table 2.5. The new acceleration distance achieved with Starshot settings is $L = 26.864$Gm, already being a significant improvement. In conclusion, the maximum stress, acceleration distance, and other critical

values were successfully replicated in this model, establishing a reliable basis for further simulations and deeper analysis. A detailed description of the obtained model setup can be seen in subsection 2.1.4.

Table 2.5: Starshot and Campbell et al. compared

	σ_{center} [MPa]	δ_{center} [m]	D [Gm]	t_l [min]
Starshot ($\phi = 30$GW)	277.25	0.0097029	**26.864**	12.36
Campbell et al.	~ 666.0	-	38.7	17.4

2.1.4. STRUCTURAL CONFIGURATION FOR LIGHTSAIL STRESS ANALYSIS

The setup used for structural analysis obtained during model validation (subsection 2.1.3) is described here. The main goal of this work is the stress analysis and response of the lightsail to uniformly applied pressure. Thus, the structural setup is essential in the correct and reliable analysis of critical parameters influencing the structure studied and its response under working conditions. Here I outline the material properties, boundary conditions, loads applied, and settings used to provide a thorough understanding and a reliable model for further use.

The authors of the validation example [61] approximate the stresses and strain and use shell physics and numerical formulas for the analysis of their structure due to the structure resembling a spherical pressure vessel. Therefore, the model is created in COMSOL® Solid Physics package with "Shell" physics applied. The applied force (to the concave area) is modeled as pressure [61].

In the Shell package, the main structure modeled does not have any thickness rendered - because of its thin assumption, the thickness is manually inserted as a number for the software to use during calculation. Views of the model are presented in Figure 2.2. The structure is fixed in space but is simply supported at the edges to allow for rotational movement [61].

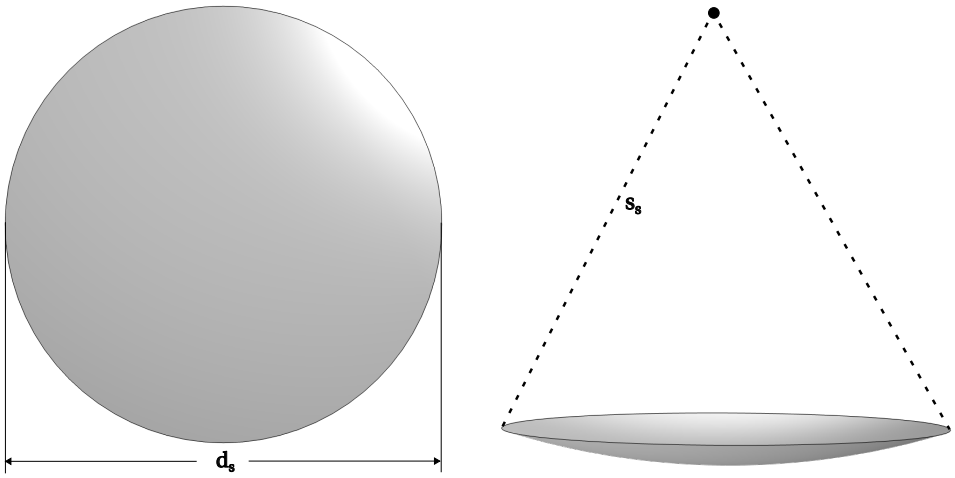

Figure 2.2: Structural setup of the curved lightsail: (left) top view with diameter d_s; (right) isometric view with curvature radius s_s

For further simulations, similar settings will be used for direct comparison purposes. Later, a nonlinear configuration will be applied (where mentioned) to provide a more realistic representation of actual stresses, strains, and deflections, as nonlinear theory is essential to model large deformation of membranes (deflection larger than half the thickness)[65][66].

2.1.5. APPLICATION OF THE TOPOLOGY OPTIMIZATION METHOD TO LIGHTSAIL DESIGN

Topology optimization has already been used for lightsail design, however, only for maximizing the reflectivity of unit cells [36], [49], [50] (subsection 1.3.5).
Up until now, for simplicity, the entire sail was treated as a circular, homogenized piece of material where stresses are evenly distributed over the entire surface. Yet, one of the most viable design considerations assumes a frame, in between which the reflective material will be suspended [61]. In the case of a lightsail structure, utilizing the topology optimization method could help achieve the middle point between robustness and maximum performance with the smallest weight.
Thus, this subsection will describe the application of topology optimization in laser-propelled spacecraft design.

BACKGROUND

The structure was set up following previous descriptions in section 2.1.
However, it proved non-trivial to apply topology optimization to a uniformly loaded shell element in COMSOL®. Under even, distributed load, a 3D curved shell structure failed to provide any results, let alone optimize. The topic is presented in more detail in chapter 5.
To overcome this limitation and obtain an indicative force distribution, a flat disk in COMSOL® 2D Plates package was simulated. The idea of this approach is to create a flat structure closely resembling that of a 3D curved disk and then map the resulting structure onto a curved surface of a shell element.

FLAT DISK TOPOLOGY OPTIMIZATION SETUP

In structural analysis, the minimization of tensile strain energy (compliance) is the most common metric to use as an objective function, which, in most general terms, is the minimization of deformations [67]. This approach suits the goal of this procedure as well, as the structure obtained will only be used indicatively in further design, rather than a perfectly optimized final device.

In COMSOL® 2D Plate Physics, a circular disk of $d_s = 3.568\text{m}$ is created ($A \approx 10\text{m}^2$). A pressure of $P = 6.67\text{Pa}$ (radiation pressure from laser power $\phi = 10\text{GW}$) is applied on the face, in the direction normal to the surface, and a fixed boundary is applied to the edges.
At this point applying geometric nonlinearity is essential, as the stresses and deformations experienced by flat thin plates at this scale surpass manageable limits (subsection 1.3.8).
Initial stress of $\sigma_0 = 1\text{GPa}$ is applied to the structure as an additional boundary condition, which represents the intrinsic internal stress of a SiN film.
For the topology optimization settings, all settings were initially configured following official software tutorials [68]. Method of Moving Asymptotes (MMA) is used, Helmholtz filtering together and hyperbolic tangent projection are enabled, and the SIMP interpolation

method is used as a means of encouraging material distribution. The initial control variable (material density) is set as $\theta_0 = 1$. All other hyperparameters were left as is.
Firstly, this basic model of a full plate is run without any optimization applied, to obtain its total elastic strain energy U_0. After this value is known, topology optimization is performed to minimize the new elastic strain energy, U, that is normalized with respect to U_0, to avoid any errors resulting from optimization tolerances of the solver [68].
The formulation is as follows [69]:

$$\begin{aligned} \min_{x} \quad & \frac{U(x)}{U_0(x)} \\ \text{subject to} \quad & \sum_i x_i \cdot A_i t_i - \frac{1}{2} V_0 \leq 0 \\ & Kd - F = 0 \\ & 0 \leq x_i \leq 1 \quad \forall i \end{aligned} \tag{2.7}$$

where x_i is the density each element i, A_i and t_i the area and thickness of each element respectively, V_0 is the original structure's volume, K is the stiffness matrix, d the displacements, and F the applied forces.

The results can be seen in Figure 2.3. As expected, the maximum deformation of the optimized structure is larger. The elastic strain energy increased, which makes the structure more compliant than its solid form, however, with the amount of removed material, thus reduced weight, the deformation difference is almost insignificant (only $\approx$ 2.4mm). The sail takes on a triangular form of 3 attachment points (Figure 2.3a), which could point to the structure's ability to resist rotation/twisting motion. Curiously, when applying a different boundary condition to the edges (simply supported edges from fixed edges), the device optimizes at 4 points of contact.

SHELL ELEMENT TOPOLOGY OPTIMIZATION

In the section above it was mentioned that topology optimization of a uniformly loaded curved shell was non-trivial and failed during initial trials. Here the problem is approached again with the results and shapes obtained from flat disk optimization.
Using the obtained material distribution forming a triangular structure, this shape is manually mapped onto a 3D curved shell element in COMSOL® 3D Shell package.
The areas were then manually prescribed material (meaning no material can be removed from those areas by the solver), and the topology optimization was run again with settings almost identical to the flat disk optimization, with the main difference being in the penalty setting, as described below.
To ensure the settings used during shell optimization are correct, and the lack of optimized material distribution is not caused by improper model setup, a validation study was performed, simulating a dome under asymmetric point loads [67], selected results of which are visible on Figure 2.4. Throughout the study it was found that default COMSOL® Topology Optimization settings, despite proven efficacy [70] (SIMP penalty factor $\rho_{\text{SIMP}} = 3$, and projection slope $\beta = 8$), were insufficient for arriving at solutions with clear division between material density $x_i \in \{0, 1\}$, resulting in significant portions of the structure with intermediate "grayscale" material distribution, here represented by shades of green and yellow.
To address this, penalty factor and projection slope values were incrementally increased to

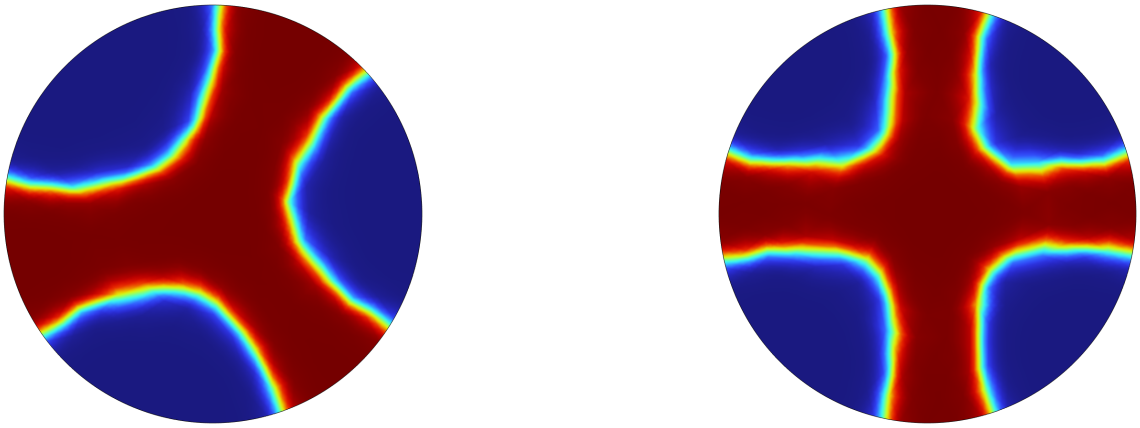

(a) (b)

Edges		δ_{center} [m]	σ_{center} [MPa]	$\frac{U}{U_0}$
Fixed	Initial	0.048995	1092.7	1.077
	Optimized	0.051389	1054.5	
Supported	Initial	0.049113	1093.2	1.073
	Optimized	0.051435	1052.5	

Figure 2.3: Resulting material distribution (red = material; blue = no material) from flat disk topology optimization for **(a)** fixed edges, and **(b)** simply supported edges; **(table)** comparison of resulting stresses and deflection from both solid and optimized disks

analyze their influence on the optimized structure. It was found that higher values push the optimizer more aggressively to solve with no middle values, resulting in the desired "0-or-1" (blue or red) material distribution. The parameters were fine-tuned until a satisfactory result was obtained, without analysis of higher ρ_{SIMP} nor β values. A more detailed study is available in Table 5.1 in chapter 5.

Thus, in further shell optimization studies, the changed parameters of $\rho_{\text{SIMP}} = 16$ and $\beta = 32$ were used to ensure proper material redistribution.

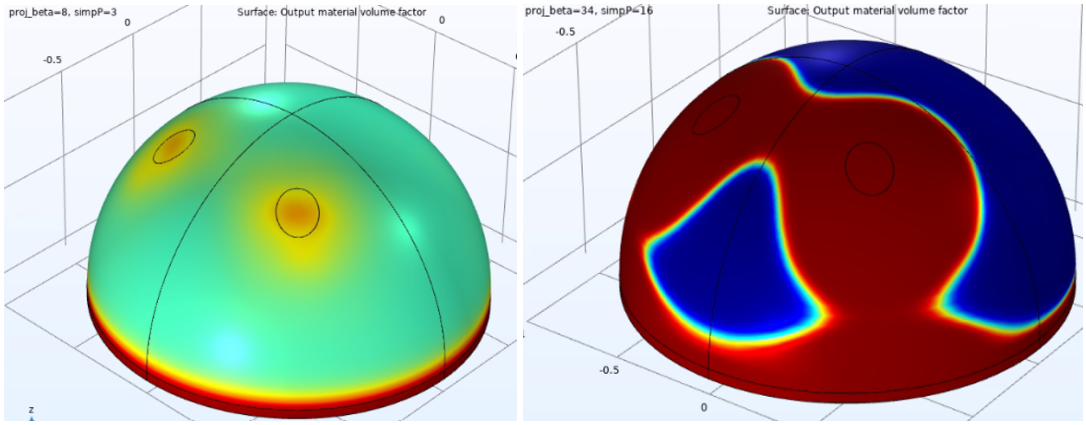

(a) $\rho_{\text{SIMP}} = 3, \quad \beta = 8$ (b) $\rho_{\text{SIMP}} = 16, \quad \beta = 34$

Figure 2.4: Asymmetrically point loaded dome [67], with prescribed material at the bottom edge, and the influence of ρ_{SIMP} and β on topology optimization of shell elements in COMSOL®. In (a) there is a significant portion of intermediate element density (green and yellow), while (b) shows material distribution much closer to desired values 0 or 1 (no material $x_i = 0$ (blue) and material $x_i = 1$ (red)).

2.2. PHOTONIC CRYSTAL REFLECTIVITY ANALYSIS

In this section, we analyze the reflectivity of the circular cavity photonic crystal. First, a literature example is replicated to validate the simulation model. Key PhC design parameters and their influences are examined. Lastly, the model for further simulations is set and described.

Building upon the previously mentioned assumptions in section 2.1, electromagnetic analysis introduces additional specific constraints to its simulations. Here we list all assumptions applicable to this section, despite some being repeated, to ensure clarity in the presentation. These are: uniformly distributed, constant, "flat top" shape, polarized laser beam; no thermal expansion nor strains, thus no change in the photonic crystal structure (i.e. constant lattice parameters); uniform material; infinite periodicity in both in-plane directions; constant wavelength $\lambda = 1550$nm; no diffraction effects; no interaction with the interstellar medium ([21], [38], [55], [57], [62], [71]).

2.2.1. REPRODUCING A PHC UNIT CELL FOR MODEL VALIDATION PURPOSES

To ensure reliable reflectivity simulation results, first a validation study is performed. The validation is performed by recreating a model used by Moura et al. (2018) [37], who manufactured single-layer 2D photonic crystal plates of different parameter combinations to maximize their reflective properties. Due to the nature of the photonic crystals in question - suspended, single layer, photonic cavity structure, silicon nitride material - it was chosen as an example most similar to the structure being analyzed in this dissertation.
The study optimized, using the FDTD method (subsection 1.3.4), 56nm and 210nm photonic crystals to be most reflective under the irradiance of a wavelength of 1550nm.
The simulated model was created by closely following the optimized configuration:

Parameters: thickness $t = 56$nm, lattice constant $a = 1526$nm, hole radius $r = 626.5$nm

A side-to-side comparison of obtained vs. original results is illustrated in Figure 2.5. The main differences between the simulations are the methods and load applied: Moura et

al. used the RCWA method to analyze the previously optimized structure closer, as well as Gaussian beam distribution to obtain their results, while this study's model was simulated using FEA in COMSOL® and uniform laser distribution. However, the obtained results still correspond well with the author's largest beam widths (dashed yellow line and light blue line) if approximated to be uniform ('flat top').
This validates the model used and proves its accuracy and reliability. For the remainder of this thesis, any subsequent PhC-light interaction will be performed on this model, with any changed parameters highlighted.

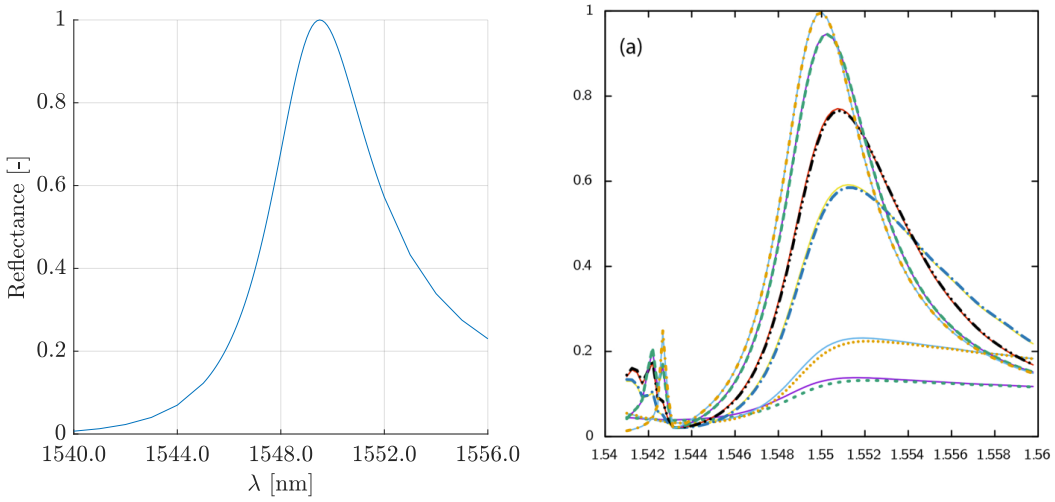

Figure 2.5: t = 56nm unit cell reproduced reflectivity spectrum: **(left)** reproduced results with "tophat", uniform irradiance; **(right)** original article reflectivity spectrum [37] with lines representing different widths of the Gaussian beam.

2.2.2. INFLUENCE OF LATTICE PITCH AND CAVITY RADIUS ON REFLECTIVITY

The main design variables of a circular unit cell cavity influencing the specifics of its wave-grating interaction are its lattice pitch (a) (the distance between cavities) and the radius of the hole (r). The relationship between them and their respective influences on reflectivity are illustrated in Figure 2.6.
It has been observed that the changing radius appears to shift the photonic crystal's reflectance peak. Specifically, increasing the radius (constant lattice pitch) leads to better reflection of shorter wavelengths. The same effect can be observed the other way around with decreasing lattice pitch (constant radius). Effectively, both increasing the lattice pitch and decreasing the radius lead to a larger surface area.

2.2.3. INFLUENCE OF UNIT CELL THICKNESS ON REFLECTIVITY

A graph presenting the influence of varying thickness on reflectivity is visible on Figure 2.6d, to provide a comprehensive understanding of all the parameters and their impact on performance.
The impact of thickness t is similar to that of lattice pitch a and radius r, meaning all 3 variables can determine the maximum reflectivity peak, shifting it to lower or higher wave-

lengths. However, t is the only parameter that exhibits influence on the broadness of the reflectivity spectrum. The visible lines for 45nm, 56nm, and 75nm get increasingly broader, pointing to thickness as a critical factor in the design for broadband reflectivity.
Designing the Lightsail involves a trade-off between thicker (thus heavier) material and achieving maximal reflectivity over the entire experienced spectrum. Although the thickness of the single-layer 2D photonic crystal is one of the main parameters influencing its optical properties, for this study it was predetermined and fixed at $t = 100$nm according to initial design guidelines ([31]) to maintain minimal mass.

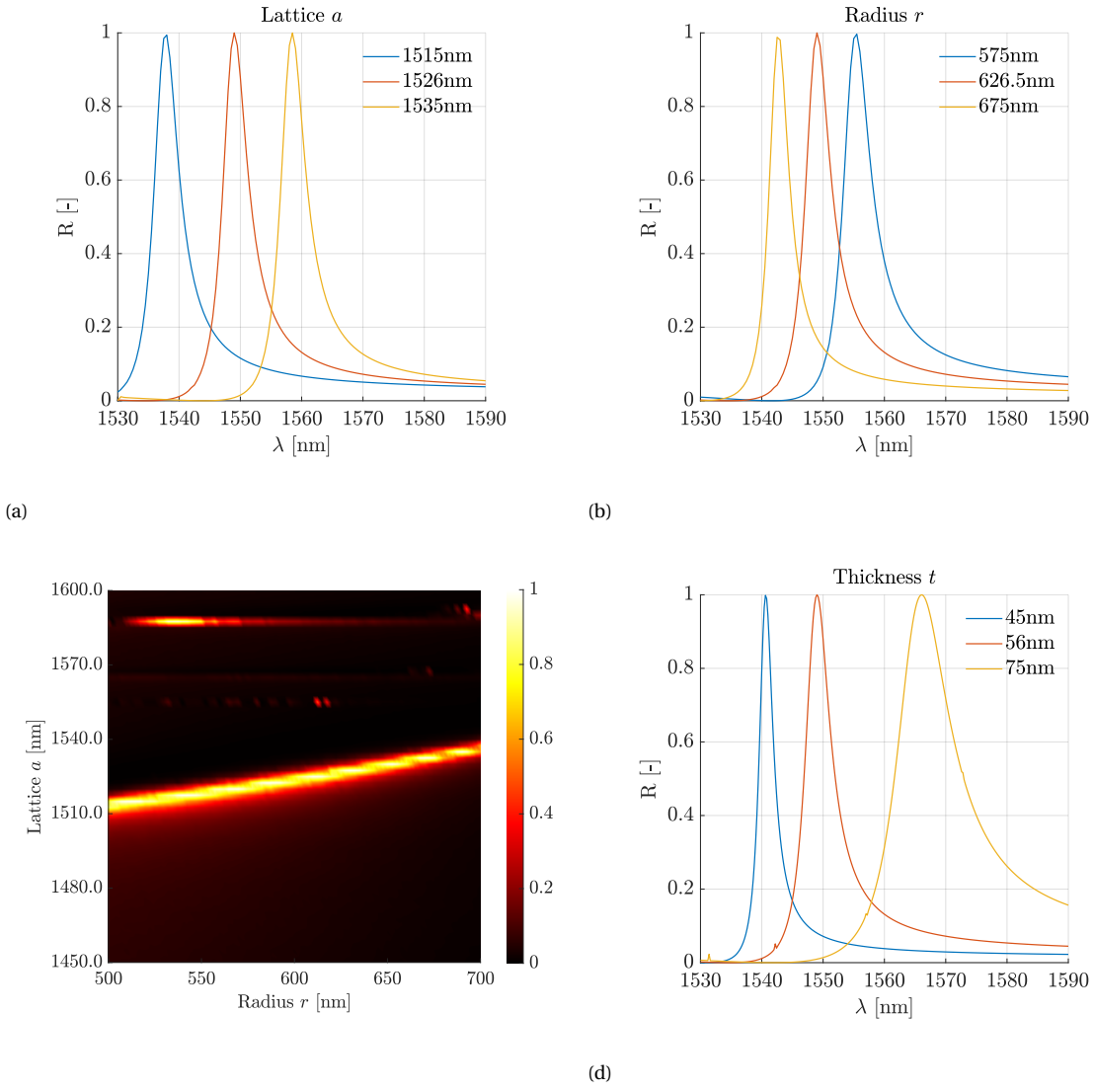

Figure 2.6: Reflectivity of different wavelengths depending on: (a) lattice pitch a; (b) radius r; and (c) relationship between a and r with respect to reflectivity; (d) influence of various thickness values on overall reflectivity with respect to the wavelength

2.2.4. SETUP FOR LIGHTSAIL PHC REFLECTIVITY ANALYSIS

A unit cell model was created to analyze the reflectivity of the initial design and assess new designs. COMSOL®Wave Optics package allows for applying periodicity conditions to the boundaries of the cell, thus simulating a photonic crystal surface composed without costly computational power. Moreover, the software facilitates detailed analysis of reflectivity and transparency, as well as their orders (directions of reflected propagation), and of the intensity of electromagnetic field. COMSOL® versions 6.1 and 5.6 were used throughout this study to perform simulations concurrently. However, after a thorough comparison of results obtained from identical models, no significant differences were identified. This ensures the reliability of sources obtained from both versions for the same study. The electromagnetic analysis is performed using Finite Element Analysis (FEA), which is the integral method within COMSOL.

This study focuses on a square lattice of circular holes, with lattice pitch (lattice constant) a and hole radius r, as well as membrane thickness t.

The model used, as well as an example mesh, are illustrated in Figure 2.7. The area above and under it is applied to model the environment surrounding the unit cell. It allows us to observe the changing and reflecting electric field, which is required for proper analysis. The applied mesh has custom sizing depending on the sensitivity of the area - the mesh applied to the unit cell itself is significantly smaller, thus more accurate, than to the rest of the model. This is done to limit the memory usage required for running the simulation while keeping the accuracy of obtained results at a satisfactory level.

To ensure the desired PhC effect, a periodicity assumption has been added to in-plane edges of the unit cell.

The direction of the incoming wave (laser) is represented by a red arrow on the left side of Figure 2.7, where a periodic port with wave excitation was applied. The incoming wave was modeled as polarized in a direction orthogonal to the direction of the traveling wave. All remaining hyperparameters were left unchanged.

The material properties for the unit cell have been taken from [63], with the real part of the index of refraction taken as $n = 2$.

The nominal values used for the model are presented in the table in Figure 2.7.

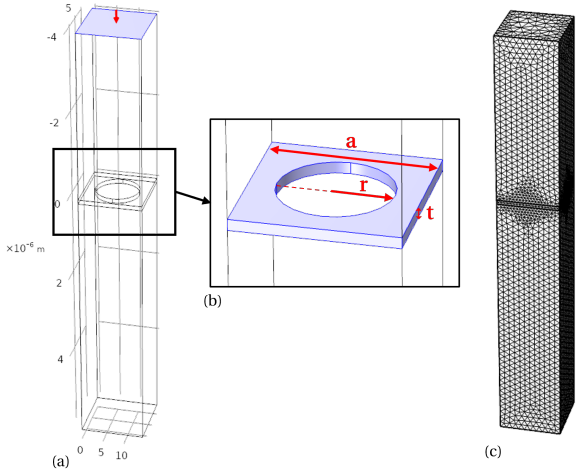

Parameter	Symbol	Values
Lattice pitch	a	1100 nm
Hole radius	r	500 nm
Thickness	t	100 nm
Wavelength	λ	1550 nm
Angle of incidence	θ	0°
Simulation region	–	10 μm

Figure 2.7: Unit cell setup: (a) Geometry of the model with a visible input port, (b) unit cell cavity, (c) Mesh of the model; (table) nominal values for the unit cell for reflectivity measurement

3

Results & Discussion

3.1. OPTIMIZING OVERALL SHAPE

The first and one of the most significant parts of the large-scale design is its large-scale shape. Apart from the material and surface used, it has the largest influence on how the laser transfers momentum to the Lightsail and accelerates it.

The structure was optimized by minimizing the objective function (here acceleration distance D), with d_s and s_s as control variables. The bounds were set up so that $s_s < \frac{d_s}{\sqrt{2}}$ to prevent the curvature from being large enough to introduce internal reflections, which may cause excessive heating and destabilizing forces [55](subsection 1.3.7). Constraints were applied to stress and displacement to prevent the linear nature of the simulation from resulting in unrealistic stretching. A pressure of $P = 6.67\text{N/m}^2$ was applied to the concave surface of the sail. The total mass of the device (including any tethers and chips) was taken as $m_{tot} = 0.002\text{kg}$ throughout the simulations.

COMSOL®'s default NELDER-MEAD method was used as it supports changing geometry and mesh [72]. All other hyperparameters were left as is. The simulation was run multiple times starting at different d_s and s_s values to explore feasible solutions and check for local minima. The results are visible in Table 3.1.

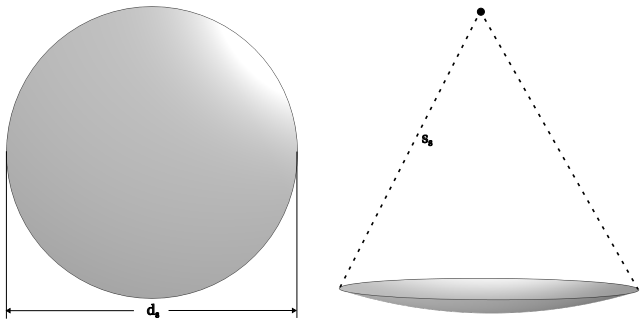

Figure 3.1: Optimized parameters

Table 3.1: Optimization of the diameter and curvature of the sail.

Starting values s_s:d_s	**Resulting** s_s	**Resulting** d_s	$\frac{s_s}{d_s}$	σ **[MPa]**	δ **[m]**	D **[Gm]**
1:1	1.2947	0.78173	1.6562	860.39	0.007	76.637
2:2	2.6862	1.6081	1.67	422.87	0.0071941	76.576
3:3	3.6633	2.1891	1.6734	311.14	0.0072134	76.563
4:4	4.5388	2.7227	1.667	249.01	0.0071513	76.590
5:5	5.2250	3.1250	1.672	217.73	0.0071978	76.569

Evidently from column $\frac{s_s}{d_s}$ the solver reaches a minimum every time the ratio between curvature and diameter reaches ~ 1.67, with minimum acceleration distance $D \approx 76.6$[Gm]. Since the ratio has the biggest impact on the acceleration distance, rather than the diameter or radius of curvature alone, the simulation was rerun with initial Starshot radius for $A_\perp = 10\text{m}^2$ and $d_s = s_s = 3.568\text{m}$ with the resultant values being:

$$s_s = 4.27m \quad d_s = 2.6m \quad A_s = 5.44m^2 \quad A_\perp = 5.31m^2 \tag{3.1}$$

where A_s is the curved area, and $A_\perp$ a "flat" (top visible) area.

Moreover, from the column indicating the stresses experienced by every structure, smaller sails experience much larger stresses than bigger structures. The smallest size analyzed here (s_s = 1.2945m, s_s = 0.78173m) experiences $\sigma \approx$ 860MPa, which is still nowhere near the ultimate tensile stress of SiN ($\sigma_T \approx$ 6000MPa) even when adjusting for commonly applied Factor of Safety FoS = 2 ($\sigma_{T,FoS} \approx$ 3000GPa). This suggests that the sail could be made even smaller to take advantage of material strength. A similar effect could be achieved by increasing the s_s thus making the structure flatter and increasing its reflectivity. Making the structure smaller allows for a larger margin in instrumentation design, however, increases the weight ratio between the sail and its payload, which could heavily impact its structural integrity and stability.

3.2. TOPOLOGY OPTIMIZATION RESULTS

Following the approach and findings described in subsection 2.1.5, prescribed material areas were applied to shell element optimization with increased penalty parameters to obtain a Lightsail backbone design with correct material distribution. With this simple application integration of methods, the optimization resulted in shapes visible on Figure 3.2. Various combinations of prescribed frames were examined to further test the optimizer. Some of the resulting shapes, like circular frames with an empty center (Figure 3.2c), or centers filled with no attachment points (Figure 3.2d), are unrealistic. Ultimately, the triangular configuration was chosen for further analysis, as other examples allow for material distribution patterns that compromise the structural integrity of the device (no attachment point) or render it useless (no support at the center).

3.3. PHC REFLECTANCE WITH RESPECT TO SURFACE CURVATURE

This section describes the resulting 2D Photonic Crystal design following the description of electromagnetic simulation setup in section 2.2.

To maximize reflectivity for wavelength λ = 1550nm the unit cell was optimized with circular cavity radius r and lattice pitch a as optimization variables, with the constraint on r applied so that it isn't larger than the lattice pitch, which in that case would result in a disconnected surface.
As visible in subsection 2.2.2 on Figure 2.6 (c), there is an area (white yellow) where the reflectivity can be maximized for a wide range of pitch and radius combinations. Interestingly, changing r has a relatively low impact on reflectivity, compared to a. From the graph, maximum reflectivity can be maintained at $a \sim 1450$ for $r \sim$ 400nm to $\sim$ 500nm. Thus, to simplify the design and eventual manufacture processes, r = 500nm is chosen as a basis for lattice pitch, which after further optimization results in a = 1454.3nm for maximum reflectivity $R = 1$.
However, the reflectivity simulation was only performed for perpendicular incidence $\theta = 0$, which will only apply to the center of the sail and a small area around it, with small angles approximated as 0. Due to the curvature of the sail, to maximize the reflectance of the sail, and with its momentum transfer capabilities, the sail would ideally exhibit high reflectivity over the entire curved surface.

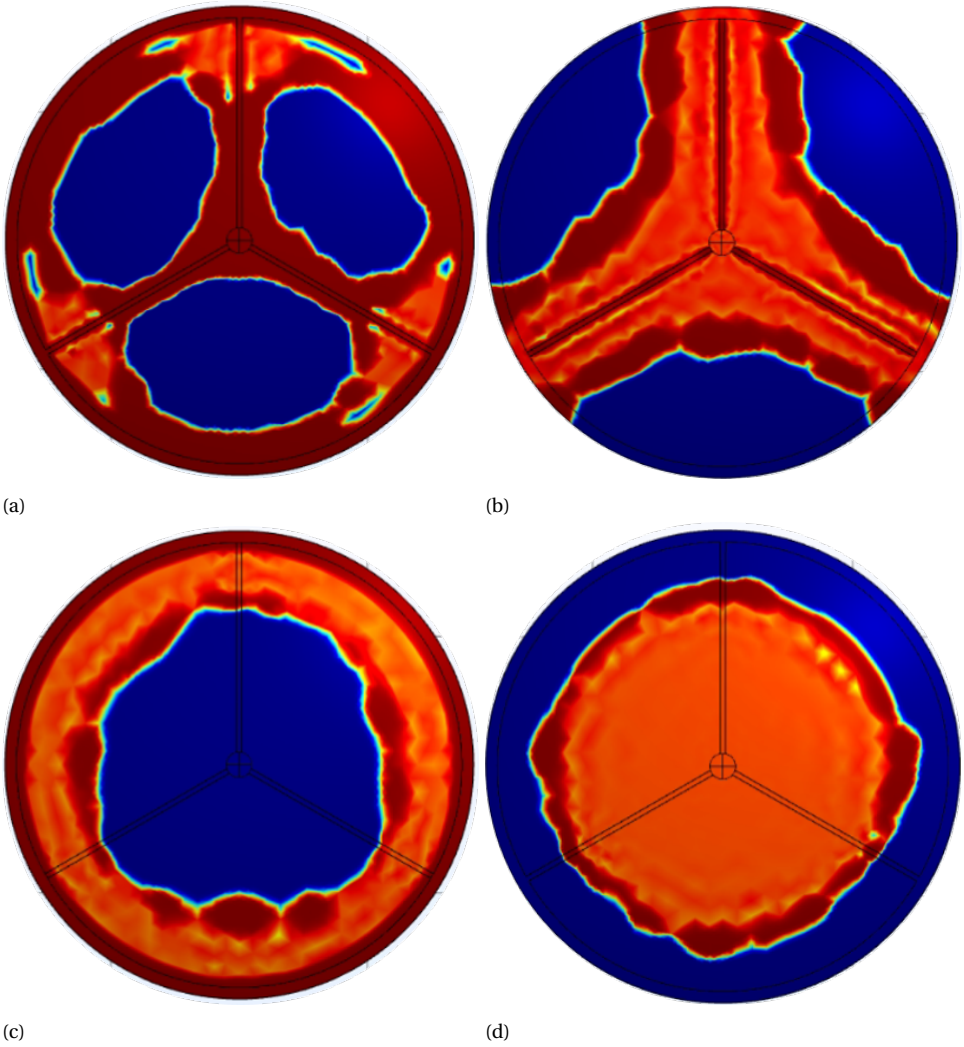

Figure 3.2: The results of uniformly loaded shell optimization with selectively prescribed material. Top view of: (a) Cross and rim, (b) cross, (c) rim, (d) no prescribed material

With the current large-scale design (section 3.1), the maximum angle that the curvature of the sail achieves is calculated with ([61]):

$$\theta_{\max} = \arcsin\left(\frac{d_s}{2s_s}\right) \approx 17.7^\circ \tag{3.2}$$

The angle is large enough to significantly influence the reflective capabilities of the sail with respect to the incident laser, which most probably won't vary its angle of incidence. Some sources [73] argue that a photonic crystal slab with circular holes in a square configuration, at constant radius and lattice pitch, can exhibit 95% reflectivity up to $\theta = 15^\circ$. Since $\theta = 15^\circ$ is close enough to the maximum angle of this sail, it offers a promising solution to the incidence angle problem. However, the slab used in their study is much thicker ($t \approx 0.55a$) compared to the thickness focused on in this thesis ($t \approx 0.07a$). Thus it is important to analyze the angle of incidence further.

The reflectivity over the entire sail can be seen on Figure 3.3a. Reflectivity drops significantly over 5° inclination, which introduces losses and lowers the overall efficiency of the

sail.
As a photonic crystal operates based on electromagnetic waves coming into interaction with a specifically designed surface, instead of a commonly understood reflectivity-off-of-a-solid-surface, any variation to its structure leads to a considerable change in (in this case) reflective properties. In the case of the angle of incident, the larger the angle, the larger the difference in photonic crystal the light "experiences" and interacts with - changing from a perfectly circular hole at perpendicular incidence to more ellipsoid holes at increasing angles, which provides a viable explanation to the drop in reflectivity.

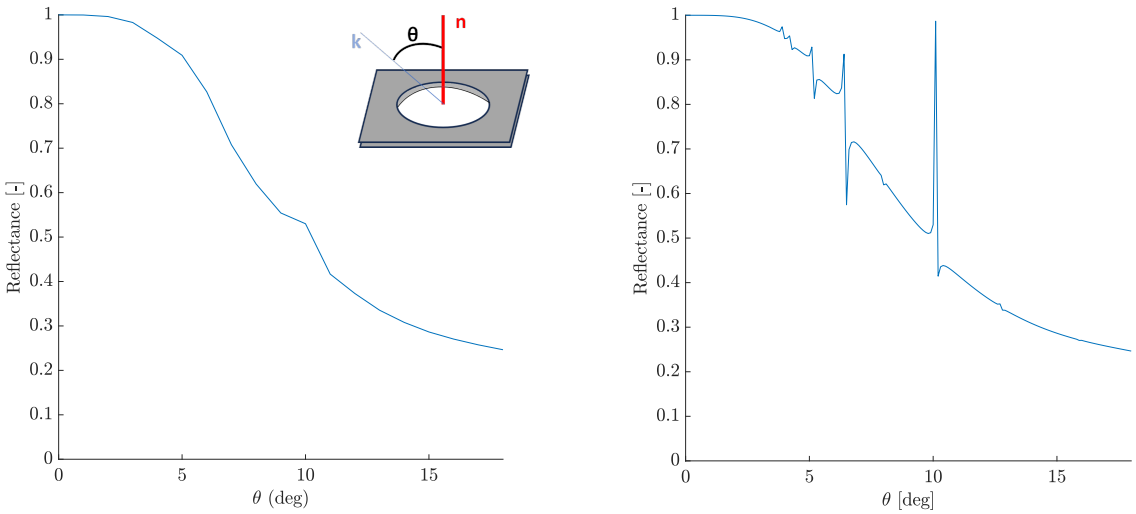

(a) (b)

Figure 3.3: Constant $a = 1453.4$nm and $r = 500$nm; (a) Basic reflectance over the sail's surface with increasing angle of incidence, and schematic of the unit cell with normal direction n, incident wave k, and the incident angle θ (1° steps), (b) Same reflectivity but with smaller angle steps (0.1°)

From the graph we can see reflectivity changes smoothly from perpendicular to increasingly inclined incidence, however at around $\theta = 10°$ there is an unexpectedly slight increase in reflectivity. Upon closer inspection, with smaller angle steps analyzed (0.1°, Figure 3.3b), despite the general smooth declining shape, multiple asymmetrical shapes appear at various angles (more detailed analysis in chapter 6). With their distinct shapes, quickly transitioning between 100% and 0% (depends on step size; 0% values not fully visible here) and back to their previous adjacent values, they are known as Fano resonances.
In photonics, Fano resonances occur from the interaction between the localized resonant mode and the extended modes of the continuum [74]–[77]. The characteristic shape of maximum and minimum amplitudes appears due to constructive and destructive interferences (between resonant and extended modes) being next to each other [77].
Fano resonances make an interesting topic and are being widely used in photonics, mainly due to their ability to create perfect mirrors or transmitters, but also due to their relatively simple design considerations (in the case of PhCs - thickness, lattice shape, and form). As visible on Figure 3.4a, the resonances "travel" with changing angle or wavelength. The smaller intensity but sharper Fano resonances eventually disappear, which could have applications in other photonic devices (like sensors and filters) [78]. However, despite the

exciting potential, a deeper analysis of Fano resonances and their application in the design of lightsail is beyond the scope of this thesis.

Due to computational limitations, it was not feasible to test the electromagnetic interaction on a large-scale curved lightsail and establish the actual impact of those phenomena. Because of their very sharp and sudden instances on the graph, it is thus assumed they have negligible impact on the overall reflectivity of the sail.

Based on previous sections on the impact of photonic crystal design variables (subsection 2.2.2), here it is hypothesized that the reflectivity of the lightsail can be maximized or maintained at unity throughout the increasing angle of incidence by adjusting the lattice pitch and/or circular hole radius. Graph examining changing lattice pitch a values versus increasing angle of incidence θ and their influence on reflectivity R can be seen on Figure 3.4b while varying r analysis is presented on Figure 3.4c.
Variable r is only a feasible design solution up to $\theta = 12°$, with no unity reflectivity achievable further up the curvature when a is kept constant and within tested limits. However, the graph of a values indicates that maximum reflectivity can be achieved throughout the entire spectrum of incident angle. Curiously, varying wavelength and radius graphs yield the same reflectivity spectrum shape, although wavelength is a more sensitive parameter. Moreover, neither change in λ nor in r have any impact on the location of Fano resonances with respect to θ.
Following this observation, only the a parameter will be used as a variable in further optical design.
Here, an optimization approach similar to the one presented at the beginning of section 3.3 was employed. However, only the lattice pitch was used as an optimization variable, with maximization of reflectivity as the objective function, and all remaining parameters remained identical.
The optimization results are presented in Figure 3.5. Especially on Figure 3.5a it's visible that to keep reflectivity at maximum the lattice pitch needs to be increased together with incident angle, with a non-linear relationship between both parameters. The line graph follows the same trend as on Figure 3.4b. Additionally Figure 3.5b clearly illustrates specific lattice pitch values required for unity reflectivity across the lightsail curvature.

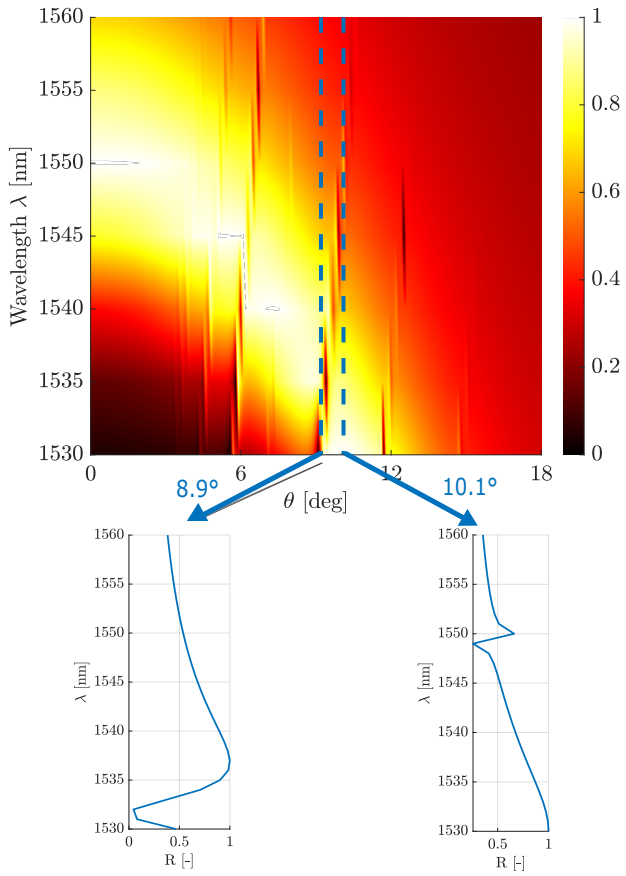

(a) Varying wavelength λ

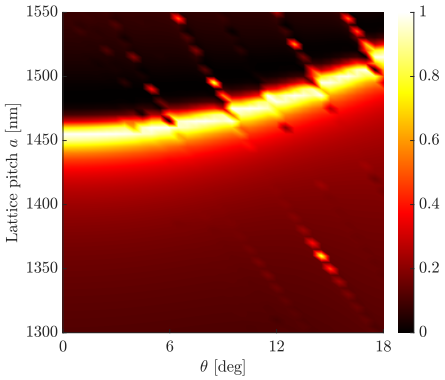

(b) Varying lattice pitch a

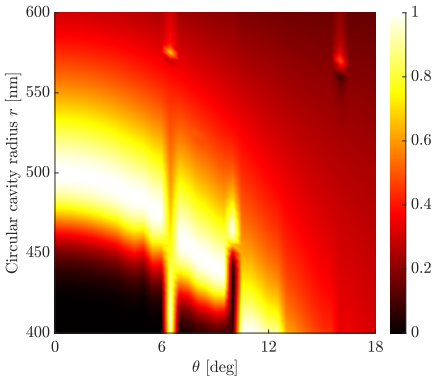

(c) Varying radius r

Figure 3.4: (a) Reflectivity spectrum for the Starshot Lightsail with changing angle and wavelength. Fano resonances are visible as "ripple" lines stretching vertically over the image; (b) and (c) same as (a) but with varying a and r respectively. The values kept at constant for relevant graphs are: t = 100nm, λ = 1550nm, a = 1454.3nm, r = 500nm

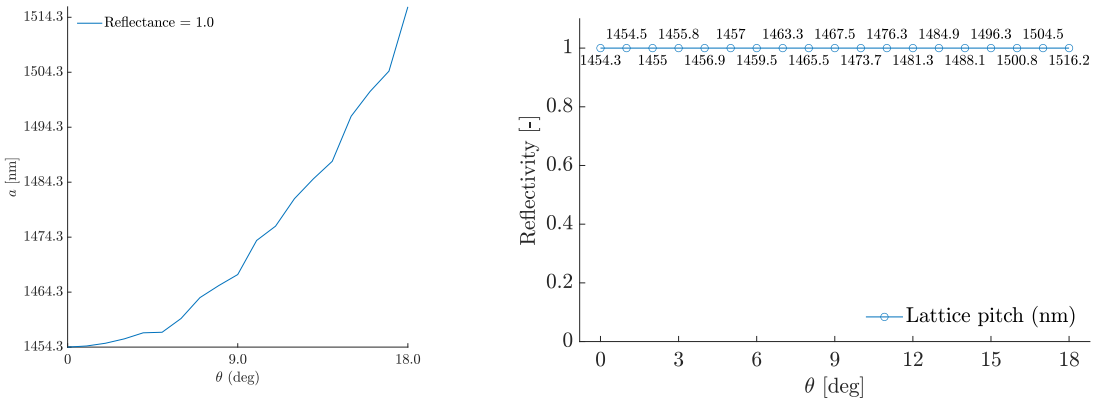

(a) (b)

Figure 3.5: (a) Lattice pitch growing with increasing angle; (b) Reflectance graph staying at maximum with a values for each angle θ

In conclusion, this analysis confirms that lattice pitch is a critical parameter in lightsail performance. By precise adjustment of lattice pitch values to increasing angle of incidence resulting from curvature, maximum reflectance can maintained across the curvature.

3.4. RESULTING DESIGN

In this section, the design considerations that were explored in previous sections are put together. The thorough analysis covered several critical factors that Lightsail's performance is comprised of, mainly stress distribution, structural integrity, and optimal reflectivity. Firstly, the material characteristics and structure of photonic crystals were explored with respect to both mechanical resistance and optical properties. Secondly, stress analysis concluded with the overall shape of the Lightsail, and topology optimization revealed the best "backbone" that ensures robustness. Lastly, different aspects of reflectivity were explored, resulting in a specific 2D PhC design for unity reflectance at perpendicular incidence, and a hypothesis was developed for maintaining maximum performance throughout the curvature and the operational environment of the sail. Based on new findings obtained throughout this analytical period, certain design sections and their procedures are revisited and updated to refine the final design.

PHC HOMOGENIZED MATERIAL

Because of updated unit cell design for reflectivity (section 3.3) the initial values presented in subsection 2.1.2 ($a \approx 1000$nm and $r \approx 450$nm) that made up the homogenized material no longer match the new requirements ($a \approx 1450$nm and $r \approx 500$nm). So the first step is to recalculate the effective properties of a homogenized material comprised of new unit cells. The radius of the cell stays the same at $r = 500$nm, however the lattice pitch changes with respect to the curvature of the sail. As the difference between smallest and largest lattice pitch values is only ~ 50nm, a representative average value is approximated at $a_{\text{average}} \approx 1474.3$nm. The results can be seen in Table 3.2 below.

Following the table and recalculating required parameters, like in Equation 2.4, the new

Table 3.2: Effective Young's Modulus values obtained in the same fashion as Table 2.2

Radius [μm]	E_{eff} [GPa]
5	271.31
10	238.33
15	232.53
25	218.49
35	215.74
50	212.35

homogenized values are:

$$E_{eff} = 200GPa \quad \rho_{PhC} = 1916kg/m^3 \quad \nu = 0.27 \tag{3.3}$$

OPTICAL DESIGN

Following analysis in section 3.3, the optical design is constructed as follows:

Material: Single layer LPCVD Silicon Nitride, with the approximate refractive index of $n \approx 2$

Structure: 2D Photonic Crystal (PhC) with uniform thickness of $t = 100nm$, patterned with circular holes in a rectangular lattice configuration

Lattice: Circular cavity radius $r = 500$nm, with the distance between holes (lattice pitch a) ranging from $a_{\theta=0^\circ} = 1454.3$nm to $a_{\theta_{\max}=17.7^\circ} = 1508.6$nm (Figure 3.6) (at $\frac{s_s}{d_s} \approx 1.64$)

These parameters ensure not only low weight, due to low thickness and cavity PhC design but also maximum theoretical performance by maximizing reflectivity over the entire curvature of the sail.

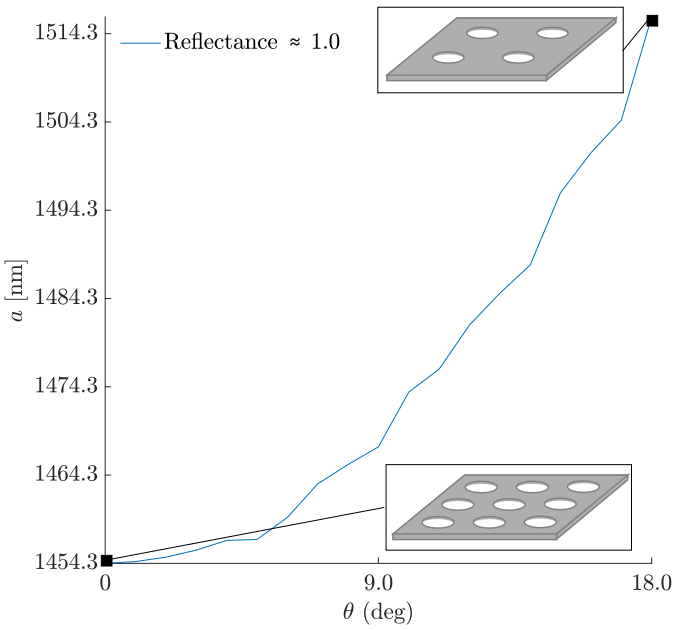

Figure 3.6: Schematic representation of the PhC structure at the center of the sail ($\theta \approx 0^\circ$) and the edge of the sail ($\theta \approx 18^\circ$), with the lattice pitch change visualized at both extremes.

STRUCTURAL DESIGN

In section 3.1 and section 3.2 the the shape and the frame of the sail were described. The general design can be seen on Figure 3.7, while the structural analysis results are presented in Table 3.3, with visual stress distribution in Figure 3.8.
Table 3.3 is divided into two main sections: linear and no with no initial stress; and nonlinear with prestress applied. Former, which (to the best of my knowledge), corresponds to settings utilized by [61], provides the parameters for direct comparison and reference, while the latter describes realistic conditions more closely ([65], [66]), with physics of large deformations applied (nonlinearity) and the initial prestress that arises in the material inherently during fabrication of thin silicon nitride layers. Table 3.3 additionally has both maximum stress at the center, for comparison with Campbell et al.'s results, and the maximum stress overall resulting from the simulation, which generally concentrates at the edges.

The nonlinear and prestressed sail experiences lower stresses, both σ_{center} and σ_{max}, as well as displacement ρ_{center}, than the linear and not prestressed sail. This is caused by the application of nonlinear physics. At larger displacements ($\delta > \frac{1}{2}t$), the material and structure become stiffer, opposing the applied forces and resulting in lower displacement when compared to the linear model. Moreover, the applied prestress causes a stiffening effect (similar to a loose sheet being pulled apart by 2 people holding it on opposite sides), which further resists deformation. Additionally, the initial tension of the sail, much larger than the applied external force, helps distribute the load more evenly across the membrane.

The effect of the rim added to the sail is best presented by Figure 3.8d. Compared to linear simulations, the stress tends to be concentrated in the rim, evident from the orange color in the triangular arms. This leaves the reflective part of the sail relatively unstressed, which has the main benefits of: structural integrity not being compromised by stress concentrating in the small areas between the holes; and the delicate photonic crystal not being strained, the deformation/lengthening of which could alter the reflective properties and reduce the efficiency (in worst case scenario the overall functionality) of the Lightsail.

Table 3.3: Final results for both Campbell et al. [61] and Breakthrough Starshot [31] laser powers, corresponding to Figure 3.8. Symbols: ϕ laser power; I laser intensity; P pressure at the center of the sail; σ_{center} stress at the center of the sail; δ_{center} displacement at the center; σ_{max} max stress experienced by the sail (edges).

	ϕ **[GW]**	I **[GW/m^2]**	**P [Pa]**	σ_{center} **[MPa]**	δ_{center} **[m]**	σ_{max} **[MPa]**
Linear	30	5.5164	37.7	847.25	0.010167	1479.6
$\sigma_0 = 0$	53	≈ 10	66.6	1497	0.017961	2614
Nonlinear	30	5.5164	37.7	795	0.0036914	909.2
$\sigma_0 = 1$**GPa**	53	≈ 10	66.6	1483.5	0.0076962	1549.1

INERTIA RELIEF

The Lightsail is initially suspended in space and pushed by a uniform force, with negligible medium resistance and no fixed edges. In simulations, applying maximum force due to laser pressure to a simply supported or clamped plate is only a simplification and overes-

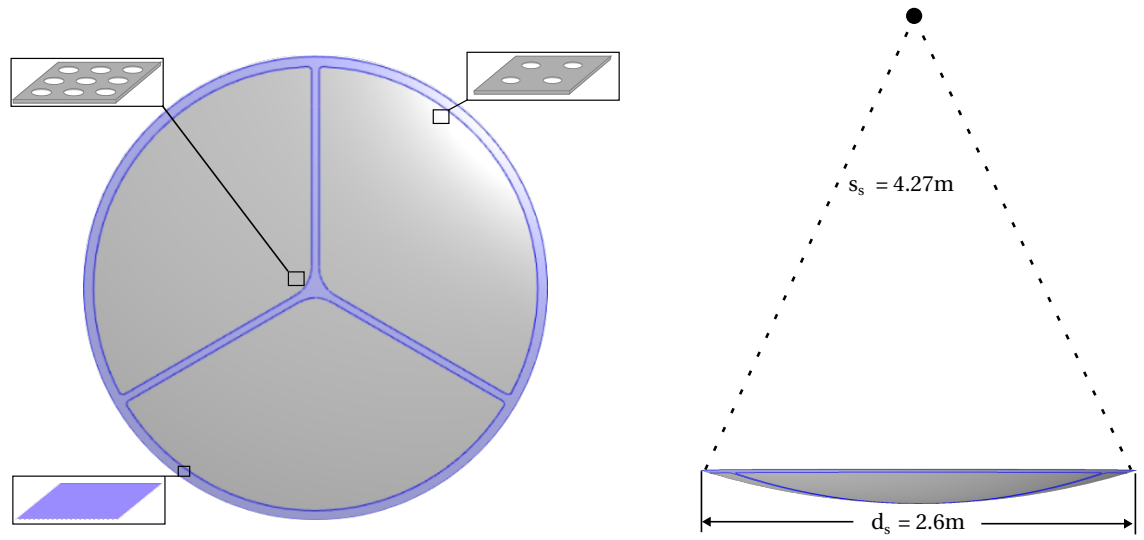

(a) (b)

Figure 3.7: Overall design and dimensions of the Lightsail

timates the maximum stresses experienced by a plate suspended in space, carrying a load (chip). To take another step towards realistic stress experienced by the sail, inertia relief was applied to the setup. This technique involved applying forces to a stationary object to mimic the effects of inertia that would act on an otherwise accelerating object.
Here, the sail and its payload both weigh $m_s = 1$g and $m_p = 1$g, respectively. It's assumed the payload weight is concentrated in the outer rim and is not being acted upon by the laser. The entire structure accelerates at $a_s = 177000\frac{m}{s^2}$ as a result of force $F = 354$N pushing on the sail. Instead of being fixed, the outer rim of $m_p = 1$g is being dragged behind, creating a reactive force of $N_r \approx 177N$ acting in the opposite direction of acceleration. To simulate these forces in a simply supported rim, the force applied to the surface of the sail is thus $N_s = 177N$, translating to a pressure $P = 33.33$Pa.
The results are visible in Table 3.4.

Table 3.4: Settings identical to Table 3.3, with applied inertia relief, effectively cutting the pressure applied in half, due to even mass between sail and payload; P_{relief} is the pressure applied due to inertia relief.

	ϕ **[GW]**	I **[GW/m^2]**	P_{relief} **[Pa]**	σ_{center} **[MPa]**	δ_{center} **[m]**	σ_{max} **[MPa]**
Linear $\sigma_0 = 0$	53	≈ 10	33.3	748.41	0.0089807	1307.0
Nonlinear $\sigma_0 = 1$GPa	53	≈ 10	33.33	687.57	0.0054613	865.16

With the stresses analyzed, the FoM values amount to:

$$D = 13.6918\text{Gm} \quad t_l = 6.2\text{min} \tag{3.4}$$

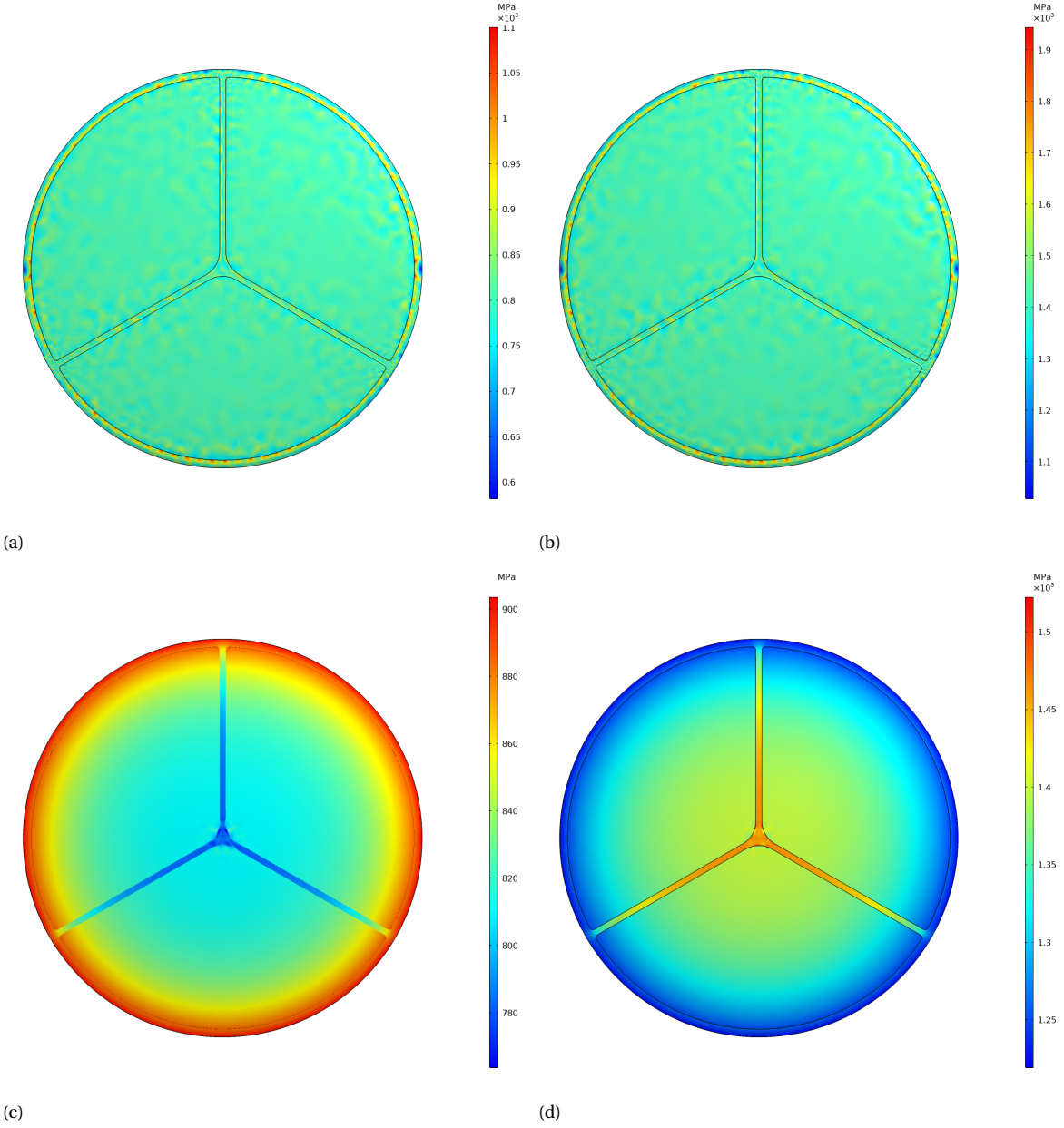

Figure 3.8: Stress distribution in various settings for either Campbell et al. [61] - $\phi = 30$GW; or Breakthrough Starshot [31] settings - $I = 10\text{GW/m}^2$ (for this sail it translates to $\phi = 53$GW):
(a) Linear, $\sigma_0 = 0$, $\phi = 30$GW; (b) Linear, $\sigma_0 = 0$, $\phi = 53$GW; (c) Nonlinear, $\sigma_0 = 1$GPa, $\phi = 30$GW; (d) Nonlinear, $\sigma_0 = 1$GPa, $\phi = 53$GW

4

CONCLUSION & RECOMMENDATIONS

4.1. CONCLUSION

In this thesis, the design of full-scale Lightsails was explored for the application of space exploration motivated by the Breakthrough Starshot challenge. Due to the size, these design considerations, that become critical at this scale are explored: their overall material and shape, stresses and deformations, enhancing performance due to reflectivity maximization over the sails curvature, and their integration into a final design.

The first and most important element influencing the performance of the sail is the material chosen. As high reflectivity is the main requirement, a review and comparison of materials commonly described in similar literature were conducted. It was found that silicon nitride (SiN) is one of the most promising materials for this application, considering its extensively researched structural and optical properties, established performance, and wide range of use in photonics. Moreover, to further reduce the weight and increase performance, a reflective structure of the sail was chosen, known as a photonic crystal (PhC) cavities, whose reflectivity can be maximized through careful calibration of its lattice.

The next important element influencing the performance of the sail is its overall shape. It lays out and determines the way stresses are distributed and how the sail deforms under the applied stresses. Moreover, flatter sails will have better overall reflectance over the entire surface area compared to more curved shapes.
Here, stress analysis and optimization of the sail were performed to not only minimize the stress, but also maximize the reflectivity, and ensure maximum efficiency. This resulted in a circular, billowing shape of a specific diameter and curvature ratio which minimizes the acceleration distance (D), a commonly used figure of merit (FOM) in Lightsail studies.
Further, to identify areas of concentrated stress, the method of topology optimization was used. Next, the findings were used to design a stronger "backbone" of the sail, where the stresses concentrate, leaving the effective reflective areas less prone to structural failure, but also less subject to deformations, which could impact the sensitive performance of the PhC.

Lastly, the reflectivity of the sail was closely explored at the unit cell level. Firstly, unit cell parameters and their influence on overall performance were identified: distance be-

tween adjacent cavities a, known as lattice pitch, the radius of circular cavities r, and the thickness of the unit cell t. All parameters were determined to impact the specific reflected wavelength independently of each other. Notably, lattice pitch a turned out to be the most sensitive parameter, while thickness t was found to significantly impact the band of the reflected wavelengths. Due to weight consideration, and to simplify the design process, the thickness of the membrane was fixed. Through optimization, a specific parameter combination was found that exhibited unity reflectivity of the target wavelength ($\lambda = 1550$nm). To counteract the effect of the curvature of the sail, which reduces the local reflective properties as the angle of incidence increases, the lattice of the sail was further optimized. It was observed that increasing the lattice pitch a with the increasing angle effectively maintained the maximum reflectivity across the entire curvature of the sail.

Finally, building upon the above findings, a comprehensive design was proposed, bringing in the optimized parameters and structural considerations. The design's structural integrity and overall performance were assessed, and its functionality and effectiveness were confirmed. A mechanical backbone was proposed through topology optimization of shell elements in COMSOL®, and it was found that stresses experienced by the sail can be minimized through simple curvature manipulation and that through careful exploration of the unit cell and precise manipulation of the lattice pitch, the effect of curvature on reflectivity, undoubtedly a significant design consideration, can be minimized, and the sail's performance enhanced.

The primary purpose of this research is to present holistic approach to large-scale Lightsail design, offering a comprehensive framework for structural and reflective aspects. We believe this work will offer a valuable foundation for future work and underline the importance of continuous innovation in this field. Moreover, the findings presented here could have an application in other areas of photonic research, from optical sensors and waveguides used in telecommunications to energy-harvesting devices such as photovoltaic cells.

4.2. RECOMMENDATIONS AND OUTLOOK

For future studies, it would be beneficial to look further into the simulations, removing some of the mentioned assumptions. This approach will ultimately lead to more realistic designs that give better and more accurate estimates of stresses and acceleration time. Although the model in this work successfully operates at the assumed wavelength of $\lambda = 1550$nm, due to time constraints it was not possible to analyze and achieve high reflectivity over the entire Doppler-shifted wavelength resulting from relativistic speeds (from 1550nm to 1900nm at $v \approx 0.2c$). One of the most important next steps would be achieving broadband reflectivity without significantly increasing weight (section 6.2). One prospective solution could be applying topology optimization to maximize reflectivity at a range of wavelengths, which could also be expanded beyond a simple single circular cavity. The method described in subsection 1.3.5 could result in novel designs that not only achieve the broadband effect but at the same time exhibit high reflectivity at steep angles.

Moreover, as the material in this thesis was homogenized by approximating material properties, it would be an improvement if further simulations were performed on actual patterned sails or even small segments of them. At such a large scale, with micro-scale el-

ements (~ $1\mu m$ cavities), FEM analysis requires remarkable computational power, which was not accessible at the time of this study.
Furthermore, regarding maintaining unity reflectivity over the angle-of-incidence spectrum, which was one of the main findings presented here: although single inclined unit cell simulations exhibit the expected reflectivity, it would be of value to perform electromagnetic analysis of relatively large segments of curved 2D photonic crystals to verify the findings further.

Lastly, to bring the findings of this thesis beyond the theoretical concepts and into practical applications, experimental validation of the results obtained throughout this thesis would be the ultimate proof of the design's effectiveness. Although producing a meter-scale, 100nm thick membrane to test the stresses remains a technical challenge, the experiments testing the angle-of-incidence design are achievable at much smaller scales, starting from flat and inclined plates to larger and curved segments.

ACKNOWLEDGEMENTS

I would like to thank Dr. R.A. Norte and Dr. M.A. Bessa for their support throughout this entire project. Despite numerous obstacles I've faced, their guidance ultimately helped me grow as a researcher and engineer. Additionally, I would like to thank the Norte Lab members for all the meetings and selfless help, which they never hesitated to offer.
Moreover, I would like to thank my family and my housemates, all of whom were with me through both ups and (many) downs, always ready to lend a hand or an ear. Special thanks to Zuz, whose bizarrely relentless support kept me afloat.
Lastly, I am grateful to A., even now, for standing by me throughout most of my university years and shaping me into the person I am today.

5

APPENDIX A: STRUCTURAL ANALYSIS

5.1. TOPOLOGY OPTIMIZATION

After COMSOL® software failed to topology optimize a uniformly loaded plate element, a general test of its capabilities was conducted.
Firstly, the variation on the classic topology optimization validation study was performed - the MBB beam [79].
Following software tutorials [68], [80], a simulation was performed in both 2D space, plate physics (as per instructions), and then in 3D space with shell physics applied. Both simulations have the thicknesses of the elements inputted numerically, instead of physically modeling the thick element. The material used was steel from COMSOL's library (E = 200GPa), the plate's geometry was 1m x 0.5m, with thickness $t = 0.01$m. The left edge was fixed, and the entire right edge was loaded with a total load of $L = 1000$N in the $-y$ direction. All other settings were applied identically to both simulations, following the aforementioned instructions.
The resulting stress distribution can be seen on Figure 5.1. Despite the exact same settings, apart from the physics applied, the topology optimization on 3D shell elements did not result in any significant material distribution, "converging" at a solution with plenty of "gray-scale" material, in effect leaving just a basic, almost uniform plate.
A reason can be found by comparing error graphs in Figure 5.1c and Figure 5.1d - the 2D plate error starts at 10^{-2} values and follows the expected course of trying to minimize it, ultimately converging at low values. For 3D shell, the starting error point is on the scale of 10^{-4}, immediately "reaching" low values and stopping the simulation. Removing the error limit causes the solver to stay on 10^{-4} error values, sometimes dropping to 10^{-8}, then stopping after reaching preset max iteration number, without any further change in topology.

To further analyze the problem, a validation study was performed. Melcher [67] performed topology optimization on a uniformly loaded shell, with 2 off-axis point loads, with a satisfactory, characteristically optimized structure (Figure 5.3a). Following the instructions presented in the thesis, material, geometry, and loading scenarios were applied and buckling tests were conducted, with corroborating stress and strain values achieved. However, after optimizing the topology for the same objective, constraints and penalty settings (SIMP $p_{\text{SIMP}} = 3$, COMSOL default $\beta = 8$), the COMSOL® shell again resulted in mostly intermediate topology, as visible in Table 5.1.

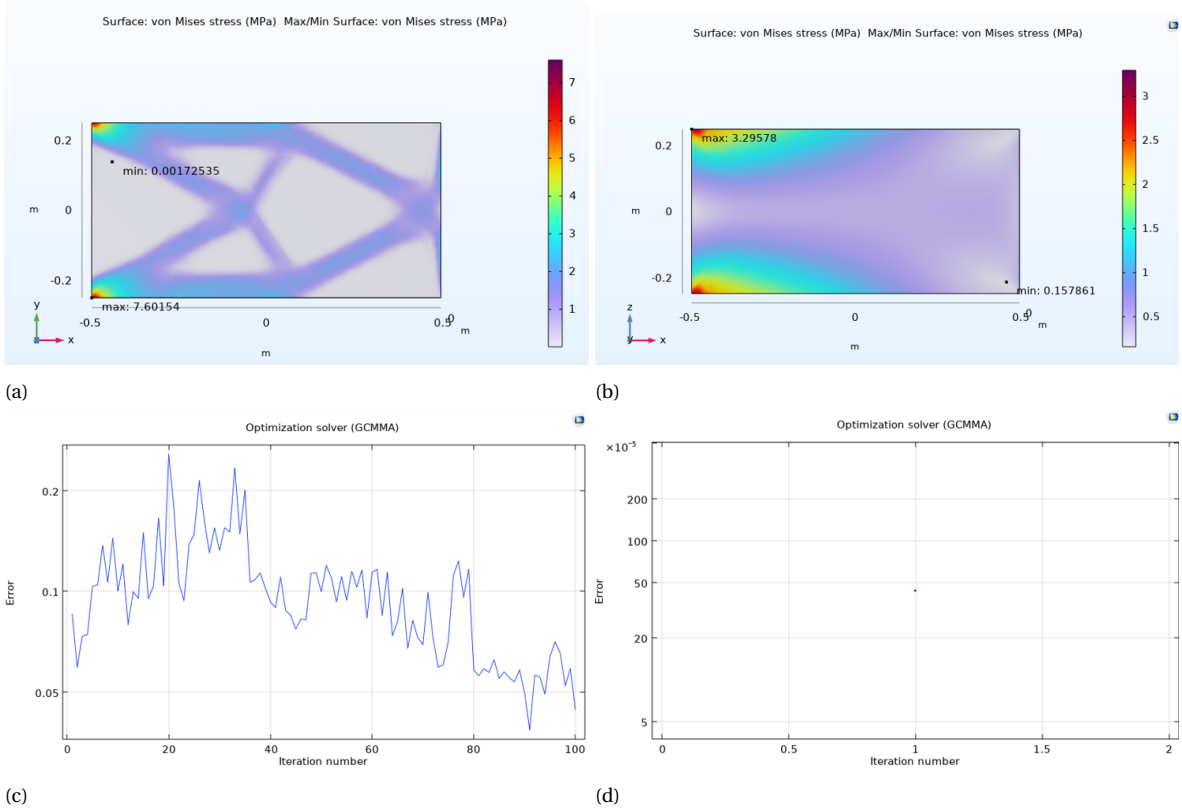

Figure 5.1: (a) 2D Plate physics beam topology optimization; (b) 3D Shell physics topology optimization; (c) 2D Plate error graph; (d) 3D Shell error graph

To try and overcome this optimization limitation, the SIMP penalty value p_{SIMP} and beta projection value β were explored. The results are visible in the remaining cells of Table 5.1. Evidently, increasing those parameters further forces the solver to arrive at element density values $x_i \in \{0,1\}$ (blue for void (0), red for material (1)), with minimal intermediary values (green and yellow).
Following these findings, the dome was optimized again with modified load points, after discussing with the author. The resultant topology not only distributes material between 0 and 1 more efficiently, but is also sufficiently similar to the figure obtained by the author. Comparison of figures on Figure 5.3. Any differences between the figures may be attributed to different softwares used (Abaqus® and COMSOL®) and certain grid shell settings, that were not necessary for this validation.

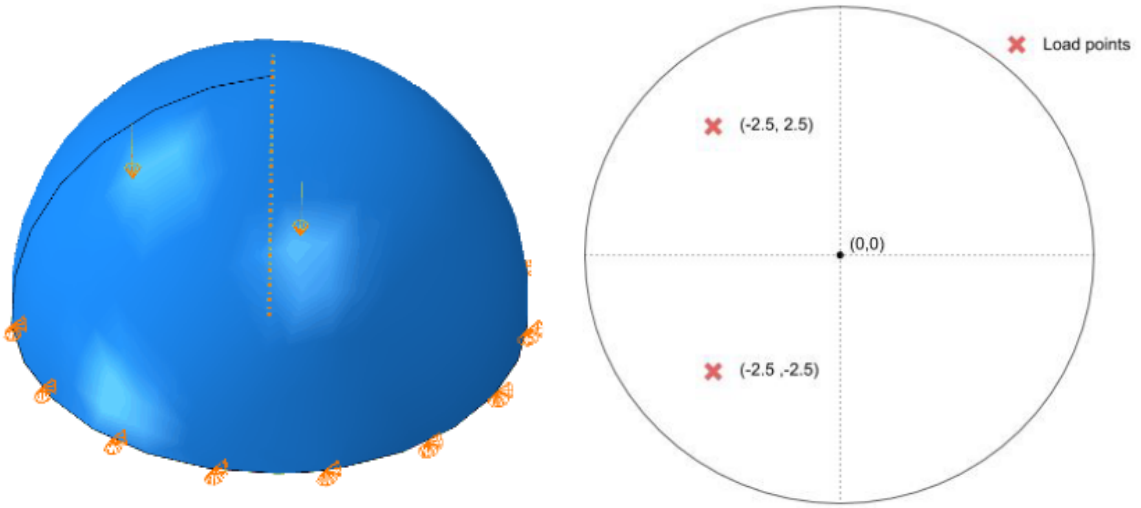

(a) (b)

Figure 5.2: (a) Full dome with asymmetric point loads; (b) Load points location[67]

Table 5.1: Results of dome optimization for different combinations of p_{SIMP} and β

	$p_{\text{SIMP}} = 3$	$p_{\text{SIMP}} = 6$	$p_{\text{SIMP}} = 8$	$p_{\text{SIMP}} = 12$	$p_{\text{SIMP}} = 16$
$\beta = 8$	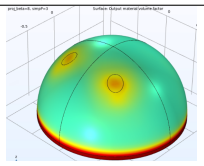	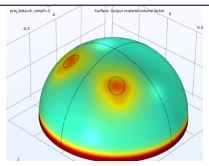	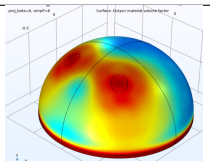		
$\beta = 12$	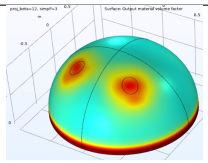	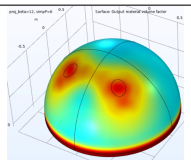	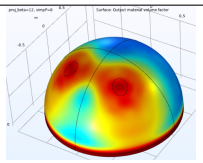		
$\beta = 18$	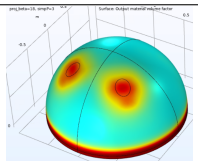	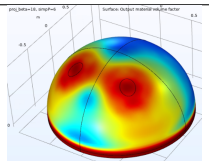	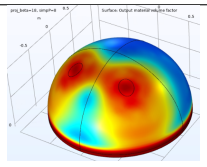	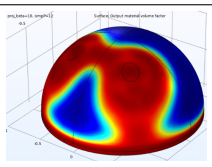	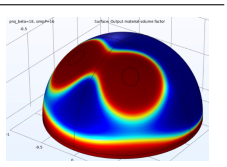
$\beta = 26$			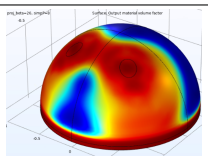	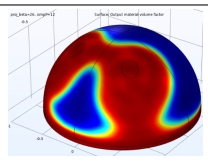	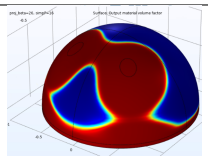
$\beta = 34$			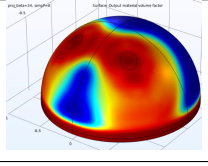	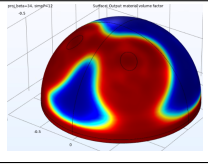	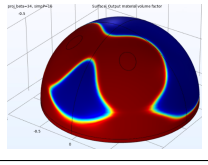

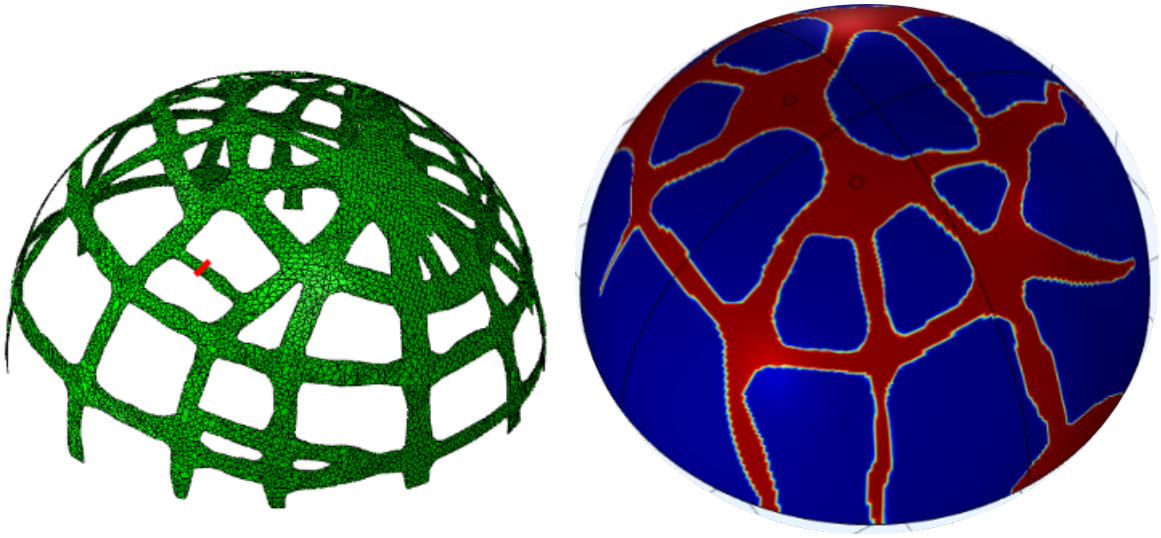

(a) (b)

Figure 5.3: (a) Melcher's optimized dome, $p_{\text{SIMP}} = 3$ [67]; (b) Optimized dome with $p_{\text{SIMP}} = 16$ and $\beta = 34$

6

APPENDIX B: ELECTROMAGNETIC ANALYSIS

6.1. FANO RESONANCE ANALYSIS

To test the apparent Fanor resonances and ensure the asymmetrical peaks do not appear due to numerical errors, several comparisons were performed between meshes, as well as software versions. On Figure 6.1a we can observe a graph similar to Figure 3.3, but with minuscule angle steps around a Fano resonance (0.01°), which points to the fact that the apparent amplitudes of the Fano resonances on the graphs depend only on the step size, and all of them can be assumed to reach values of $R = 0$ and $R = 1$. Small steps were not taken throughout the entire spectrum due to the computational power and simulation time required. The steps used in the main text graphs sufficiently point to the location of the resonances.

On Figure 6.1b we see a direct version comparison between COMSOL® v6.1 and v5.6. Although the amplitudes differ, the locations of the resonances are identical. We argue that, as mentioned in the paragraph above, the amplitude differences are purely numerical and could be matched with suitably small steps. The remaining graphs Figure 6.1c and Figure 6.1d showcase the impact of the mesh sizing on reflectivity and the Fano resonances in different software versions. The "mesh" value represents the standard mesh sizing used throughout the thesis, multiplied by different values to achieve various sizing; "mesh fine" is one of the automatic COMSOL® sizes, without control over specific element sizes, which also happened to be mesh containing largest element sizes, hence the reflectivity spectrum not matching the rest of the lines. Despite the differences in meshes and overall reflectivity for size "mesh fine", Fano resonances appeared in the same locations along the analysed curvature.

This effectively concludes that the location of Fano resonances along the angle of incidence does not depend on mesh size or version of the software.

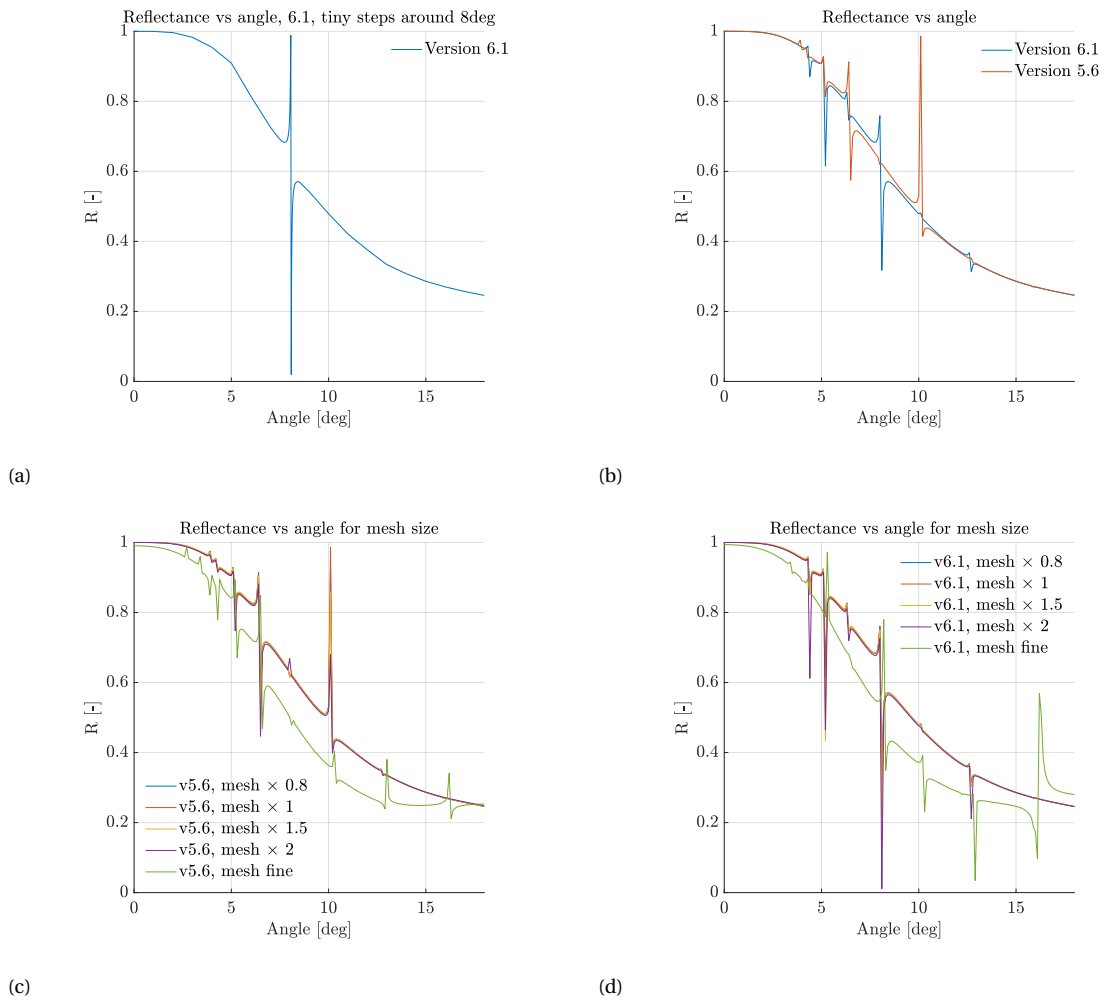

Figure 6.1: Various Fano resonance analyses with mesh and version comparison: (a) Fano resonance reaching minimum and maximum values with small steps (0.01°) around the angle of interest; (b) Version comparison; (c) and (d) impact of mesh sizing on the apparent amplitudes of Fano resonances.

6.2. REFLECTANCE OVER DOPPLER-SHIFTED SPECTRUM

Due to the relativistic velocities, the wavelength experienced by the Lightsail will increase, in what is known as Redshift, from $\lambda_{\beta=0.0} = 1550$nm to $\lambda_{\beta=0.2} = 1900$nm. For the sail to be efficient throughout its acceleration phase, it must exhibit high reflectivity over the entire spectrum. Unfortunately, achieving broadband reflectivity with thin single-layer 2D photonic crystals is nontrivial. To the best of my knowledge, this hasn't been achieved for SiN without a significant increase in thickness. Even then it doesn't cover a ~ 400nm wavelength shift. On Figure 6.2 we can see the reflectivity spectrum of the perpendicular unit cell used in the thesis. Its adjacent graph presents the reflectivity of a unit cell adjusted to reflect the broad range of $\lambda = 1550 - 1900$nm. While the reflected wavelengths do not exhibit high reflectivity over the entire spectrum, the graph aims to demonstrate the possibility of achieving broader reflectivity around wavelength 1550nm by changing the parameters.

Figure 6.3 displays graphs of reflectivity spectra based on design guidelines from various authors. Despite different settings, broadband is still mainly achieved through thicker

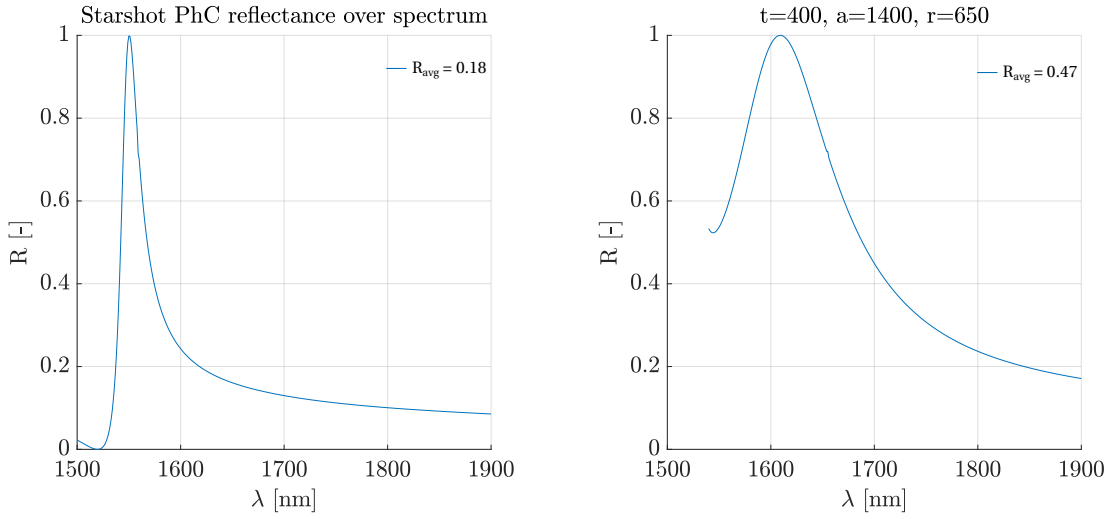

(a) $D = 77.6623\text{Gm}$ $t_l = 35.84\text{min}$ $m_s = 1\text{g}$

(b) $D = 124\text{Gm}$ $t_l = 57.2\text{min}$ $m_s = 3.3\text{g}$

Figure 6.2: Broadband reflectivity with average reflectivity over the spectrum: (a) the perpendicular unit cell used in the thesis; (b) an example adjusted unit cell (Parameters in the title)

membranes, and the obtained spectrum lines appear to follow the same shapes of either a peak followed by a smooth dip (example on Figure 6.3a), or a "saddle" distribution (clearly visible on Figure 6.3d). This might suggest that for the current configuration, these are the achievable broadband spectra. These studies, as well as this thesis, focus on the configuration of circular cavities in a rectangular configuration. However, expanding the design space to include various cavity shapes (e.g. ellipse) and configurations (e.g. hexagonal) could achieve high reflectivity broadband without significantly increasing thickness and weight.

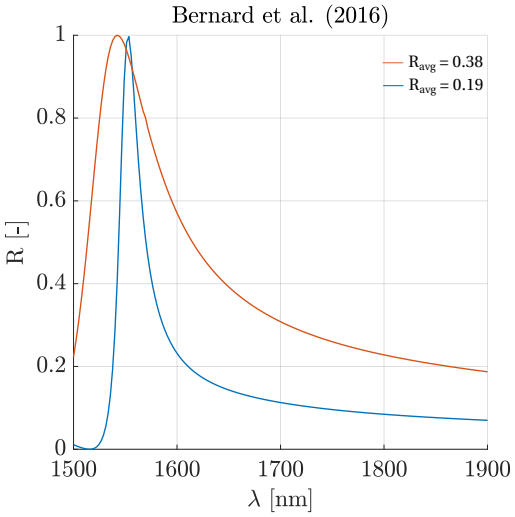

(a) (orange) $D = 48.7$Gm $t_l = 22.5$min $m_s = 1.7$g
(blue) $D = 70.4$Gm $t_l = 32.48$min $m_s = 0.9$g

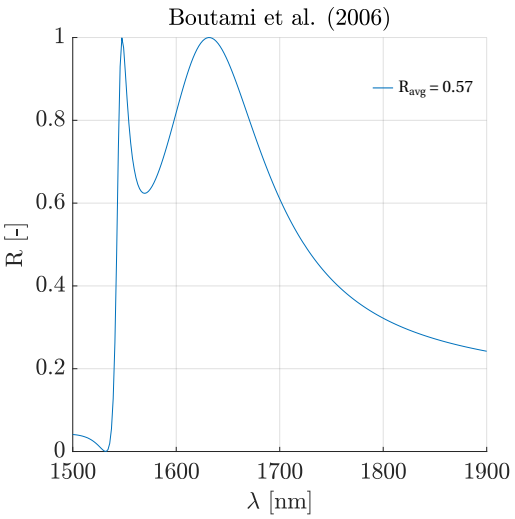

(b) $D = 47.8$Gm $t_l = 22.05$min $m_s = 3$g

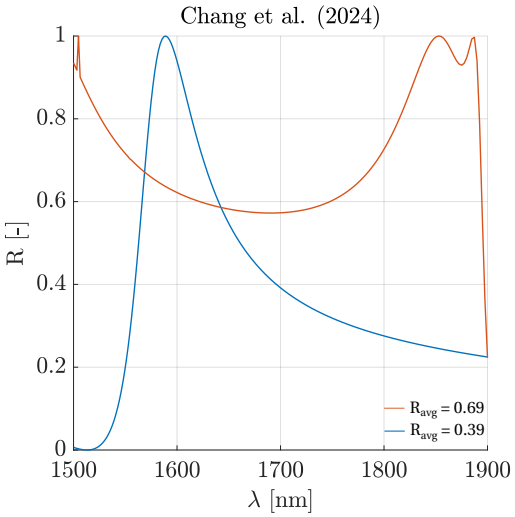

(c) (orange) $D = 76.7$Gm $t_l = 35.4$min $m_s = 6.8$g
(blue) $D = 50.48$Gm $t_l = 23.3$min $m_s = 1.9$g

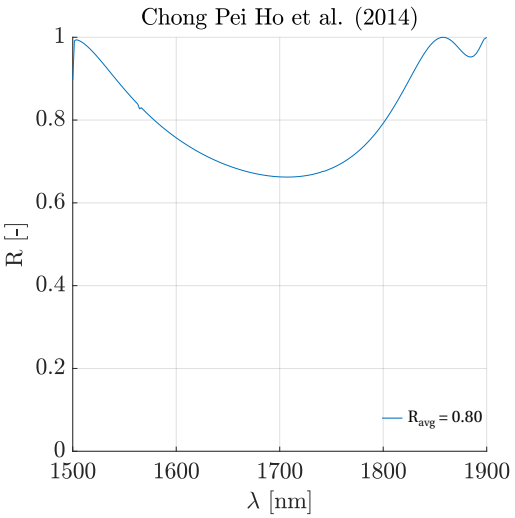

(d) $D = 60.43$Gm $t_l = 27.9$min $m_s = 6.1$g

Figure 6.3: Setup following various authors, with average reflectivity over the entire spectrum: (a) [81] a = 1339nm, r = 522nm, t = 200nm, (blue) a = 1470nm, r = 554.5nm, t = 100nm; (b) [82] a = 1340nm, r = 566.4nm, t = 420nm; (c) [83] (orange) a = 1365nm, r = 500nm, t = 721nm, (blue) t = 721nm; (d) [84] a = 1425nm, $r = 0.395$a, $t = 0.513$a

BIBLIOGRAPHY

[1] "History of Flight." (), [Online]. Available: https://www.grc.nasa.gov/www/k-12/UEET/StudentSite/historyofflight.html.

[2] S. Loff. "Apollo 11 Mission Overview," NASA. (2015), [Online]. Available: http://www.nasa.gov/mission_pages/apollo/missions/apollo11.html.

[3] NASA. "In Depth | Parker Solar Probe," NASA Solar System Exploration. (2022), [Online]. Available: https://solarsystem.nasa.gov/missions/parker-solar-probe/in-depth.

[4] mars.nasa.gov. "Mars 2020 Perseverance Rover - NASA." (), [Online]. Available: https://mars.nasa.gov/mars2020/.

[5] "In Depth | Akatsuki," NASA Solar System Exploration. (), [Online]. Available: https://solarsystem.nasa.gov/missions/akatsuki/in-depth.

[6] "In Depth | Hayabusa 2," NASA Solar System Exploration. (), [Online]. Available: https://solarsystem.nasa.gov/missions/hayabusa-2/in-depth.

[7] A. J. published. "China's Yutu 2 rover still rolling after nearly 4 years on moon's far side," Space.com. (Sep. 18, 2022), [Online]. Available: https://www.space.com/china-yutu-2-rover-still-alive-moon-far-side.

[8] T. Greicius. "Juno - Mission to Jupiter," NASA. (2015), [Online]. Available: http://www.nasa.gov/mission_pages/juno/main/index.html.

[9] "Voyager." (), [Online]. Available: https://voyager.jpl.nasa.gov/.

[10] "NASA: Artemis," NASA. (), [Online]. Available: https://www.nasa.gov/specials/artemis/index.html.

[11] "Dragonfly," NASA. (), [Online]. Available: https://www.nasa.gov/subject/17128/dragonfly.

[12] "Moon to Mars Overview | NASA." (), [Online]. Available: https://www.nasa.gov/topics/moon-to-mars/overview.

[13] "Mars." (), [Online]. Available: https://www.esa.int/Science_Exploration/Human_and_Robotic_Exploration/Exploration/Mars.

[14] "SpaceX," SpaceX. (), [Online]. Available: http://www.spacex.com.

[15] L. Crane. "NASA's Parker Solar Probe has gone faster than any spacecraft ever," New Scientist. (2021), [Online]. Available: https://www.newscientist.com/article/2276358-nasas-parker-solar-probe-has-gone-faster-than-any-spacecraft-ever/.

[16] "The 20 Closest Stars - Hipparcos - Cosmos." (), [Online]. Available: https://www.cosmos.esa.int/web/hipparcos/closest-stars.

[17] "Shuttle technical facts." (), [Online]. Available: https://www.esa.int/Science_Exploration/Human_and_Robotic_Exploration/Space_Shuttle/Shuttle_technical_facts.

[18] D. Lev, R. M. Myers, K. M. Lemmer, J. Kolbeck, H. Koizumi, and K. Polzin, "The technological and commercial expansion of electric propulsion," *Acta Astronautica*, vol. 159, pp. 213–227, Jun. 1, 2019, ISSN: 0094-5765. DOI: 10.1016/j.actaastro.2019.03.058. [Online]. Available: https://www.sciencedirect.com/science/article/pii/S0094576518319672.

[19] C. Bruno and C. Dujarric, "In-space nuclear propulsion," *Acta Astronautica*, 7th IAA Symposium on Realistic Advanced Scientific Space MissionsAosta, Italy, July 2011, vol. 82, no. 2, pp. 159–165, Feb. 1, 2013, ISSN: 0094-5765. DOI: 10.1016/j.actaastro.2012.08.022. [Online]. Available: https://www.sciencedirect.com/science/article/pii/S0094576512003323.

[20] G. Vulpetti, "Antimatter propulsion for space exploration," *Journal of the British Interplanetary Society*, vol. 39, no. 9, pp. 391–409, 1986.

[21] N. Kulkarni, P. Lubin, and Q. Zhang, "Relativistic Spacecraft Propelled by Directed Energy," *The Astronomical Journal*, vol. 155, no. 4, p. 155, Mar. 16, 2018, ISSN: 1538-3881. DOI: 10.3847/1538-3881/aaafd2. [Online]. Available: https://iopscience.iop.org/article/10.3847/1538-3881/aaafd2.

[22] A. Ashkin, "Applications of Laser Radiation Pressure," *Science*, vol. 210, no. 4474, pp. 1081–1088, Dec. 5, 1980. DOI: 10.1126/science.210.4474.1081. [Online]. Available: https://www.science.org/doi/abs/10.1126/science.210.4474.1081.

[23] F. A. Tsander, "From a Scientific Heritage," *NASA Technical Translation TTF-541*, 1967.

[24] R. L. Forward, "Roundtrip interstellar travel using laser-pushed lightsails," *Journal of Spacecraft and Rockets*, vol. 21, no. 2, pp. 187–195, Mar. 1984, ISSN: 0022-4650, 1533-6794. DOI: 10.2514/3.8632. [Online]. Available: https://arc.aiaa.org/doi/10.2514/3.8632.

[25] "IKAROS Small Scale Solar Powered Sail Demonstration Satellite | Spacecraft," ISAS. (), [Online]. Available: https://www.isas.jaxa.jp/en/missions/spacecraft/current/ikaros.html.

[26] S. Gong and M. Macdonald, "Review on solar sail technology," *Astrodynamics*, vol. 3, no. 2, pp. 93–125, Jun. 2019, ISSN: 2522-008X, 2522-0098. DOI: 10.1007/s42064-019-0038-x. [Online]. Available: http://link.springer.com/10.1007/s42064-019-0038-x.

[27] "JAXA | IKAROS Mission Overview." (), [Online]. Available: https://global.jaxa.jp/countdown/f17/overview/ikaros_e.html.

[28] "Breakthrough Initiatives." (), [Online]. Available: https://breakthroughinitiatives.org/about.

[29] "Breakthrough Initiatives." (), [Online]. Available: https://breakthroughinitiatives.org/initiative/3.

[30] "Breakthrough Initiatives." (), [Online]. Available: https://breakthroughinitiatives.org/challenges/3.

[31] H. A. Atwater, A. R. Davoyan, O. Ilic, *et al.*, "Materials challenges for the Starshot lightsail," *Nature Materials*, vol. 17, no. 10, pp. 861–867, Oct. 2018, ISSN: 1476-1122, 1476-4660. DOI: 10.1038/s41563-018-0075-8. [Online]. Available: https://www.nature.com/articles/s41563-018-0075-8.

[32] M. Williams and U. Today. "Exactly how we would send our first laser-powered probe to Alpha Centauri." (), [Online]. Available: https://phys.org/news/2018-12-laser-powered-probe-alpha-centauri.html.

[33] J. Bergmann, M. Heusinger, G. Andrä, and F. Falk, "Temperature dependent optical properties of amorphous silicon for diode laser crystallization," *Optics Express*, vol. 20, no. 106, A856–A863, Nov. 5, 2012, ISSN: 1094-4087. DOI: 10.1364/OE.20.00A856. [Online]. Available: https://opg.optica.org/oe/abstract.cfm?uri=oe-20-S6-A856.

[34] P. Lubin, *A Roadmap to Interstellar Flight*, 2016. arXiv: 1604.01356 [astro-ph, physics:physics]. [Online]. Available: http://arxiv.org/abs/1604.01356.

[35] Z. Shen, Y. Xia, Y. Liu, Y. Ding, and C. Zhao, "Protection of Materials from Space Radiation Environments on Spacecraft," *IOP Conference Series: Materials Science and Engineering*, vol. 585, no. 1, p. 012 089, Jul. 2019, ISSN: 1757-899X. DOI: 10.1088/1757-899X/585/1/012089. [Online]. Available: https://dx.doi.org/10.1088/1757-899X/585/1/012089.

[36] W. Jin, W. Li, M. Orenstein, and S. Fan, "Inverse Design of Lightweight Broadband Reflector for Relativistic Lightsail Propulsion," *ACS Photonics*, vol. 7, no. 9, pp. 2350–2355, Sep. 16, 2020, ISSN: 2330-4022, 2330-4022. DOI: 10.1021/acsphotonics.0c00768. [Online]. Available: https://pubs.acs.org/doi/10.1021/acsphotonics.0c00768.

[37] J. P. Moura, R. A. Norte, J. Guo, C. Schäfermeier, and S. Gröblacher, "Centimeter-scale suspended photonic crystal mirrors," *Optics Express*, vol. 26, no. 2, pp. 1895–1909, Jan. 22, 2018, ISSN: 1094-4087. DOI: 10.1364/OE.26.001895. [Online]. Available: https://opg.optica.org/oe/abstract.cfm?uri=oe-26-2-1895.

[38] K. V. Myilswamy, A. Krishnan, and M. L. Povinelli, "Photonic crystal lightsail with nonlinear reflectivity for increased stability," *Optics Express*, vol. 28, no. 6, p. 8223, Mar. 16, 2020, ISSN: 1094-4087. DOI: 10.1364/OE.387687. [Online]. Available: https://opg.optica.org/abstract.cfm?URI=oe-28-6-8223.

[39] H.-T. Tung and A. Davoyan, "Light-Sail Photonic Design for Fast-Transit Earth Orbital Maneuvering and Interplanetary Flight," version 1, 2021. DOI: 10.48550/ARXIV.2107.09121. [Online]. Available: https://arxiv.org/abs/2107.09121.

[40] O. Ilic, C. M. Went, and H. A. Atwater, "Nanophotonic Heterostructures for Efficient Propulsion and Radiative Cooling of Relativistic Light Sails," *Nano Letters*, vol. 18, no. 9, pp. 5583–5589, Sep. 12, 2018, ISSN: 1530-6984, 1530-6992. DOI: 10.1021/acs.nanolett.8b02035. [Online]. Available: https://pubs.acs.org/doi/10.1021/acs.nanolett.8b02035.

[41] J. Brewer, M. F. Campbell, P. Kumar, *et al.*, "Multiscale Photonic Emissivity Engineering for Relativistic Lightsail Thermal Regulation," *Nano Letters*, vol. 22, no. 2, pp. 594–601, Jan. 26, 2022, ISSN: 1530-6984, 1530-6992. DOI: 10.1021/acs.nanolett.1c03273. [Online]. Available: https://pubs.acs.org/doi/10.1021/acs.nanolett.1c03273.

[42] R. Gao, M. D. Kelzenberg, Y. Kim, O. Ilic, and H. A. Atwater, "Optical Characterization of Silicon Nitride Metagrating-Based Lightsails for Self-Stabilization," *ACS Photonics*, vol. 9, no. 6, pp. 1965–1972, Jun. 15, 2022, ISSN: 2330-4022, 2330-4022. DOI: 10.1021/acsphotonics.1c02022. [Online]. Available: https://pubs.acs.org/doi/10.1021/acsphotonics.1c02022.

[43] G. Santi, G. Favaro, A. J. Corso, *et al.*, "Multilayers for directed energy accelerated lightsails," *Communications Materials*, vol. 3, no. 1, p. 16, Dec. 2022, ISSN: 2662-4443. DOI: 10.1038/s43246-022-00240-8. [Online]. Available: https://www.nature.com/articles/s43246-022-00240-8.

[44] R. V. Nair and R. Vijaya, "Photonic crystal sensors: An overview," *Progress in Quantum Electronics*, vol. 34, no. 3, pp. 89–134, May 1, 2010, ISSN: 0079-6727. DOI: 10.1016/j.pquantelec.2010.01.001. [Online]. Available: https://www.sciencedirect.com/science/article/pii/S0079672710000029.

[45] Z. A. Kudyshev, A. V. Kildishev, V. M. Shalaev, and A. Boltasseva, "Optimizing Startshot Lightsail Design: A Generative Network-Based Approach," *ACS Photonics*, vol. 9, no. 1, pp. 190–196, Jan. 19, 2022, ISSN: 2330-4022, 2330-4022. DOI: 10.1021/acsphotonics.1c01352. [Online]. Available: https://pubs.acs.org/doi/10.1021/acsphotonics.1c01352.

[46] M. Paulsen, L. T. Neustock, S. Jahns, J. Adam, and M. Gerken, "Simulation methods for multiperiodic and aperiodic nanostructured dielectric waveguides," *Optical and Quantum Electronics*, vol. 49, no. 3, p. 107, Mar. 2017, ISSN: 0306-8919, 1572-817X. DOI: 10.1007/s11082-017-0918-6. [Online]. Available: http://link.springer.com/10.1007/s11082-017-0918-6.

[47] M. K. Callens, H. Marsman, L. Penninck, *et al.*, "RCWA and FDTD modeling of light emission from internally structured OLEDs," *Optics Express*, vol. 22, no. S3, A589, May 5, 2014, ISSN: 1094-4087. DOI: 10.1364/OE.22.00A589. [Online]. Available: https://opg.optica.org/oe/abstract.cfm?uri=oe-22-S3-A589.

[48] I. Andonegui and A. J. Garcia-Adeva, "The finite element method applied to the study of two-dimensional photonic crystals and resonant cavities," *Optics Express*, vol. 21, no. 4, p. 4072, Feb. 25, 2013, ISSN: 1094-4087. DOI: 10.1364/OE.21.004072. [Online]. Available: https://opg.optica.org/oe/abstract.cfm?uri=oe-21-4-4072.

[49] L. Norder, "Lightsail design with neural optimization of topology," p. 83, 2022.

[50] S. Hoyer, J. Sohl-Dickstein, and S. Greydanus. "Neural reparameterization improves structural optimization." arXiv: 1909.04240 [cs, stat]. (Sep. 13, 2019), [Online]. Available: http://arxiv.org/abs/1909.04240, preprint.

[51] W. Jin, W. Li, C. Khandekar, M. Orenstein, and S. Fan, *Laser cooling assisted thermal management of lightsails*, Jun. 10, 2022. arXiv: 2206.05383 [physics]. [Online]. Available: http://arxiv.org/abs/2206.05383.

[52] X. Zhu, Q. Su, W. Feng, and F. Li, "Anti-Stokes shift luminescent materials for bio-applications," *Chemical Society Reviews*, vol. 46, no. 4, pp. 1025–1039, Feb. 20, 2017, ISSN: 1460-4744. DOI: 10.1039/C6CS00415F. [Online]. Available: https://pubs.rsc.org/en/content/articlelanding/2017/cs/c6cs00415f.

[53] E. Popova, M. Efendiev, and I. Gabitov, "On the stability of a space vehicle riding on an intense laser beam: E. POPOVA, M. EFENDIEV AND I. GABITOV," *Mathematical Methods in the Applied Sciences*, vol. 40, no. 4, pp. 1346–1354, Mar. 15, 2017, ISSN: 01704214. DOI: 10.1002/mma.4282. [Online]. Available: https://onlinelibrary.wiley.com/doi/10.1002/mma.4282.

[54] Z. Manchester and A. Loeb, "Stability of a Light Sail Riding on a Laser Beam," *The Astrophysical Journal*, vol. 837, no. 2, p. L20, Mar. 7, 2017, ISSN: 2041-8213. DOI: 10.3847/2041-8213/aa619b. arXiv: 1609.09506 [astro-ph, physics:physics]. [Online]. Available: http://arxiv.org/abs/1609.09506.

[55] R. Gao, M. D. Kelzenberg, and H. A. Atwater, "Dynamically Stable Radiation Pressure Propulsion of Flexible Lightsails for Interstellar Exploration," version 1, 2023. DOI: 10.48550/ARXIV.2301.08894. [Online]. Available: https://arxiv.org/abs/2301.08894.

[56] J. Siegel, A. Wang, S. G. Menabde, M. A. Kats, M. S. Jang, and V. W. Brar, *Self-stabilizing laser sails based on optical metasurfaces*, Mar. 21, 2019. arXiv: 1903.09077 [cond-mat, physics:physics]. [Online]. Available: http://arxiv.org/abs/1903.09077.

[57] O. Ilic and H. A. Atwater, "Self-stabilizing photonic levitation and propulsion of nanostructured macroscopic objects," *Nature Photonics*, vol. 13, no. 4, pp. 289–295, Apr. 2019, ISSN: 1749-4885, 1749-4893. DOI: 10.1038/s41566-019-0373-y. [Online]. Available: http://www.nature.com/articles/s41566-019-0373-y.

[58] M. M. Salary and H. Mosallaei, "Inverse Design of Diffractive Relativistic Meta-Sails via Multi-Objective Optimization," *Advanced Theory and Simulations*, vol. 4, no. 6, p. 2 100 047, Jun. 2021, ISSN: 2513-0390, 2513-0390. DOI: 10.1002/adts.202100047. [Online]. Available: https://onlinelibrary.wiley.com/doi/10.1002/adts.202100047.

[59] M. Z. Rafat, H. R. Dullin, B. T. Kuhlmey, *et al.*, *Self-stabilization of light sails by damped internal degrees of freedom*, Jun. 21, 2021. arXiv: 2106.10961 [physics]. [Online]. Available: http://arxiv.org/abs/2106.10961.

[60] J. Zhang, N. Wu, A. Tong, and Y. Liu, "Structural dynamic responses of a stripped solar sail subjected to solar radiation pressure," *Chinese Journal of Aeronautics*, vol. 33, no. 8, pp. 2204–2211, Aug. 2020, ISSN: 10009361. DOI: 10.1016/j.cja.2020.05.003. [Online]. Available: https://linkinghub.elsevier.com/retrieve/pii/S1000936120301886.

[61] M. F. Campbell, J. Brewer, D. Jariwala, A. Raman, and I. Bargatin, "Relativistic light sails need to billow," *Nano Letters*, vol. 22, no. 1, pp. 90–96, Jan. 12, 2022, ISSN: 1530-6984, 1530-6992. DOI: 10.1021/acs.nanolett.1c03272. arXiv: 2105.10849 [astro-ph, physics:physics]. [Online]. Available: http://arxiv.org/abs/2105.10849.

[62] T. Hoang, A. Lazarian, B. Burkhart, and A. Loeb, "The Interaction of Relativistic Spacecrafts with the Interstellar Medium," *The Astrophysical Journal*, vol. 837, no. 1, p. 5, Mar. 1, 2017, ISSN: 0004-637X, 1538-4357. DOI: 10.3847/1538-4357/aa5da6. [Online]. Available: https://iopscience.iop.org/article/10.3847/1538-4357/aa5da6.

[63] "LPCVD SiN." (), [Online]. Available: https://www.mit.edu/~6.777/matprops/lpcvd_sin.htm.

[64] H. Kaushal, V. Jain, and S. Kar, *Free Space Optical Communication* (Optical Networks). New Delhi: Springer India, 2017, ISBN: 978-81-322-3691-7. DOI: 10.1007/978-81-322-3691-7. [Online]. Available: http://link.springer.com/10.1007/978-81-322-3691-7.

[65] S. P. Timoshenko and S. Woinowsky-Krieger, *Theory of Plates and Shells* (McGraw-Hill Classic Textbook Reissue), 2. ed., [Nachdr.] New York: McGraw-Hill, 1987, 580 pp., ISBN: 978-0-07-064779-4.

[66] R. Kao and N. Perrone, "Large deflections of axisymmetric circular membranes," *International Journal of Solids and Structures*, vol. 7, no. 12, pp. 1601–1612, Dec. 1, 1971, ISSN: 0020-7683. DOI: 10.1016/0020-7683(71)90001-1. [Online]. Available: https://www.sciencedirect.com/science/article/pii/0020768371900011.

[67] G. E.) Melcher, "Topology optimized hemispherical shell under asymmetric loads," Thesis, Massachusetts Institute of Technology, 2020. [Online]. Available: https://dspace.mit.edu/handle/1721.1/127315.

[68] "Performing Topology Optimization in the COMSOL® Software," COMSOL. (), [Online]. Available: https://www.comsol.com/video/topology-optimization-in-comsol-multiphysics.

[69] Y. Jiang, K. Zhan, J. Xia, and M. Zhao, "Topology Optimization for Minimum Compliance with Material Volume and Buckling Constraints under Design-Dependent Loads," *Applied Sciences*, vol. 13, no. 1, p. 646, Jan. 2023, ISSN: 2076-3417. DOI: 10.3390/app13010646.

[70] M. P. Bendsøe and O. Sigmund, "Material interpolation schemes in topology optimization," *Archive of Applied Mechanics (Ingenieur Archiv)*, vol. 69, no. 9-10, pp. 635–654, Nov. 22, 1999, ISSN: 0939-1533, 1432-0681. DOI: 10.1007/s004190050248. [Online]. Available: http://link.springer.com/10.1007/s004190050248.

[71] A. Macchi, "Theory of light sail acceleration by intense lasers: An overview," *High Power Laser Science and Engineering*, vol. 2, e10, Apr. 1, 2014, ISSN: 2095-4719, 2052-3289. DOI: 10.1017/hpl.2014.13. [Online]. Available: https://www.cambridge.org/core/product/identifier/S2095471914000139/type/journal_article.

[72] "About Derivative-Free Solvers." (), [Online]. Available: https://doc.comsol.com/6.2/doc/com.comsol.help.opt/opt_ug_solver.8.08.html.

[73] V. Lousse, W. Suh, O. Kilic, S. Kim, O. Solgaard, and S. Fan, "Angular and polarization properties of a photonic crystal slab mirror," *Optics Express*, vol. 12, no. 8, pp. 1575–1582, Apr. 19, 2004, ISSN: 1094-4087. DOI: 10.1364/OPEX.12.001575. [Online]. Available: https://opg.optica.org/oe/abstract.cfm?uri=oe-12-8-1575.

[74] Z. Qiang, H. Yang, L. Chen, H. Pang, Z. Ma, and W. Zhou, "Fano filters based on transferred silicon nanomembranes on plastic substrates," *Applied Physics Letters*, vol. 93, no. 6, p. 061 106, Aug. 11, 2008, ISSN: 0003-6951, 1077-3118. DOI: 10.1063/1.2971199. [Online]. Available: https://pubs.aip.org/apl/article/93/6/061106/322875/Fano-filters-based-on-transferred-silicon.

[75] A. Singh Chadha, D. Zhao, S. Chuwongin, Z. Ma, and W. Zhou, "Polarization- and angle-dependent characteristics in two dimensional photonic crystal membrane reflectors," *Applied Physics Letters*, vol. 103, no. 21, p. 211 107, Nov. 18, 2013, ISSN: 0003-6951, 1077-3118. DOI: 10.1063/1.4832221. [Online]. Available: https://pubs.aip.org/apl/article/103/21/211107/25054/Polarization-and-angle-dependent-characteristics.

[76] W. Suh and S. Fan, "All-pass transmission or flattop reflection filters using a single photonic crystal slab," *Applied Physics Letters*, vol. 84, no. 24, pp. 4905–4907, Jun. 14, 2004, ISSN: 0003-6951, 1077-3118. DOI: 10.1063/1.1763221. [Online]. Available: https://pubs.aip.org/apl/article/84/24/4905/508099/All-pass-transmission-or-flattop-reflection.

[77] W. Zhou, D. Zhao, Y.-C. Shuai, *et al.*, "Progress in 2D photonic crystal Fano resonance photonics," *Progress in Quantum Electronics*, vol. 38, no. 1, pp. 1–74, Jan. 2014, ISSN: 00796727. DOI: 10.1016/j.pquantelec.2014.01.001. [Online]. Available: https://linkinghub.elsevier.com/retrieve/pii/S0079672714000020.

[78] M. F. Limonov, M. V. Rybin, A. N. Poddubny, and Y. S. Kivshar, "Fano resonances in photonics," *Nature Photonics*, vol. 11, no. 9, pp. 543–554, Sep. 2017, ISSN: 1749-4885, 1749-4893. DOI: 10.1038/nphoton.2017.142. [Online]. Available: https://www.nature.com/articles/nphoton.2017.142.

[79] M. P. Bendsøe and N. Kikuchi, "Generating optimal topologies in structural design using a homogenization method," *Computer Methods in Applied Mechanics and Engineering*, vol. 71, no. 2, pp. 197–224, Nov. 1988, ISSN: 00457825. DOI: 10.1016/0045-7825(88)90086-2. [Online]. Available: https://linkinghub.elsevier.com/retrieve/pii/0045782588900862.

[80] "Performing Topology Optimization with the Density Method," COMSOL. (), [Online]. Available: https://www.comsol.com/blogs/performing-topology-optimization-with-the-density-method.

[81] S. Bernard, C. Reinhardt, V. Dumont, Y.-A. Peter, and J. C. Sankey. "Etch-Tuning and Design of Silicon Nitride Photonic Crystal Reflectors." arXiv: 1609.00858 [cond-mat, physics:physics]. (Sep. 8, 2016), [Online]. Available: http://arxiv.org/abs/1609.00858, preprint.

[82] S. Boutami, B. Bakir, H. Hattori, *et al.*, "Broadband and compact 2-D photonic crystal reflectors with controllable polarization dependence," *IEEE Photonics Technology Letters*, vol. 18, no. 7, pp. 835–837, Apr. 2006, ISSN: 1041-1135. DOI: 10.1109/LPT.2006.871833. [Online]. Available: http://ieeexplore.ieee.org/document/1608178/.

[83] J. Chang, W. Ji, X. Yao, A. J. Van Run, and S. Gröblacher, "Broadband, High-Reflectivity Dielectric Mirrors at Wafer Scale: Combining Photonic Crystal and Metasurface Architectures for Advanced Lightsails," *Nano Letters*, vol. 24, no. 22, pp. 6689–6695, Jun. 5, 2024, ISSN: 1530-6984, 1530-6992. DOI: 10.1021/acs.nanolett.4c01374. [Online]. Available: https://pubs.acs.org/doi/10.1021/acs.nanolett.4c01374.

[84] Chong Pei Ho, P. Pitchappa, P. Kropelnicki, Jian Wang, Yuandong Gu, and Chengkuo Lee, "Development of Polycrystalline Silicon Based Photonic Crystal Membrane for Mid-Infrared Applications," *IEEE Journal of Selected Topics in Quantum Electronics*, vol. 20, no. 4, pp. 94–100, Jul. 2014, ISSN: 1077-260X, 1558-4542. DOI: 10.1109/JSTQE.2013.2294463. [Online]. Available: http://ieeexplore.ieee.org/document/6680624/.